Science Bulletin **Manuscript Template**

Possible obliquity-forced warmth in southern Asia during the last glacial stage

Cheng Zhao[1,2,3*], Eelco J. Rohling[4,5], Zhengyu Liu[6], Xiaoqiang Yang[7], Enlou Zhang[1,2], Jun Cheng[8], Zhonghui Liu[9], Zhisheng An[2,10], Xiangdong Yang[1], Xiaoping Feng[1], Xiaoshuang Sun[1], Can Zhang[1], Tianlong Yan[1], Hao Long[1,2], Hong Yan[2,10], Zicheng Yu[11,12], Weiguo Liu[2,10], Shi-Yong Yu[13], Ji Shen[1,3*]

[1]State Key Laboratory of Lake Science and Environment, Nanjing Institute of Geography and Limnology, Chinese Academy of Sciences, Nanjing 210008, China.
[2]CAS Center for Excellence in Quaternary Science and Global Change, Xian 710061, China.
[3]School of Geography and Ocean Science, Nanjing University, Nanjing 210023, China.
[4]Research School of Earth Sciences, the Australian National University, Canberra ACT 2601, Australia.
[5]Ocean and Earth Science, University of Southampton, National Oceanography Centre, Southampton SO14 3ZH, United Kingdom.
[6]Department of Geography, Ohio State University, 154 N. Oval Mall, Columbus, OH 43210, USA.
[7]Department of Earth Sciences, Sun Yat-Sen University, Guanghzou 510275, China.
[8]Laboratory of Meteorological Disaster, Ministry of Education (KLME)/Joint International Research Laboratory of Climate and Environment Change (ILCEC)/Collaborative Innovation Center on Forecast and Evaluation of Meteorological Disasters (CIC-FEMD), Nanjing University of Information Science and Technology, Nanjing 210044, China.
[9]Department of Earth Sciences, University of Hong Kong, Hong Kong, China.
[10]State Key Laboratory of Loess and Quaternary Geology, Institute of Earth Environment, Chinese Academy of Sciences, Xi'an 710061, China.
[11]Department of Earth and Environmental Sciences, Lehigh University, Bethlehem, Pennsylvania 18015, USA.
[12]Institute for Peat and Mire Research, School of Geographical Sciences, Northeast Normal University, Changchun 130024, China.
[13]School of Geography, Geomatics, and Planning, Jiangsu Normal University, Xuzhou, Jiangsu 221116, China.

* Corresponding authors:

Email: czhao@niglas.ac.cn (Cheng Zhao); jishen@nju.edu.cn (Ji Shen).

Abstract

Orbital-scale global climatic changes during the late Quaternary are dominated by high-latitude influenced ~100,000-year global ice-age cycles and monsoon influenced ~23,000-year low-latitude hydroclimate variations. However, the shortage of highly-resolved land temperature records remains a limiting factor for achieving a comprehensive understanding of long-term low-latitude terrestrial climatic changes. Here, we report paired mean annual air temperature (MAAT) and monsoon intensity proxy records over the past 88,000 years from Lake Tengchongqinghai in southwestern China. While summer monsoon intensity follows the ~23,000-year precession beat found also in previous studies, we identify previously unrecognized warm periods at 88,000-71,000 and 45,000-22,000 years ago, with 2-3 °C amplitudes that are close to our recorded full glacial-interglacial range. Using advanced transient climate simulations and comparing with forcing factors, we find that these warm periods in our MAAT record probably depends on local annual mean insolation, which is controlled by Earth's ~41,000-year obliquity cycles and is anti-phased to annual mean insolation at high latitudes. The coincidence of our identified warm periods and intervals of high-frequent dated archaeological evidence highlights the importance of temperature on anatomically modern humans in Asia during the last glacial stage.

Keywords: Southern Asia, lake sediments, brGDGTs, annual temperature, the last glacial stage, obliquity forcing

1 Introduction

Southern Asia, including India monsoon-influenced southwestern China, was a major habitat and dispersal route for anatomically modern *Homo sapiens* following their "out of Africa" migration ~100,000 years ago (100 ka) [1-2]. Characterizing climate changes in this monsoon-influenced region, in particularly over the last glacial cycle, may therefore provide important climatic context to this dispersal [2]. So far, long-term monsoon hydroclimate variations in broader Asian monsoon region have been established from a range of different records [3-5], showing strong 23,000-year precession cycles driven by boreal summer insolation [4]. Meanwhile, nearby low-latitude sea-surface temperature (SST) reconstructions display the "classical" ~100,000-year ice-age cycles [6-8], due to the influences of greenhouse-gas (GHG) forcing and showing in-phase with high-latitude climates [6]. Yet, hardly any sufficiently resolved and dated, and well-quantified land-based annual mean temperature records exist for Indian monsoon-influenced Southern Asia through the last glacial stage and until the present. For example, the most recent syntheses of global temperature over the last deglaciation [9-10] and Holocene [11-12] contain only three summer temperature records in southwestern China. These indicate an overall Holocene summer cooling associated with declining Holocene boreal summer insolation [13-14], with associated reduction in Holocene summer monsoon intensities [3-5]. In contrast to this summer season trend, recent climate simulations indicate that many low-latitude land areas, including Indian-monsoon influenced Southern Asia, experienced an increase in Holocene annual mean temperatures [15]. This contrast between summer and annual mean temperature trends is likely dominated by similarly contrasting changes in Holocene summer and annual mean insolation [13-15], although increasing GHGs could also play a role [16]. According

to astronomical calculations, annual mean insolation variations in low latitudes are modulated by obliquity, and therefore (1) are opposite to those at high latitudes, and (2) fluctuate with a fundamentally different periodicity than the precession-dominated variations in summer insolation [17]. Hence, detailed reconstructions of annual mean temperature records in Southern Asia are needed to obtain a comprehensive view of long-term climate changes. This, in turn, may offer valuable climatic context for understanding developments in *Homo sapiens* in Asia (Fig. S1 online) through the last glacial stage.

Branched glycerol dialkyl glycerol tetraethers (brGDGTs) are membrane-spanning lipids produced by heterotrophic bacteria containing two C_{28} alkyl chains with 4-6 methyl substituents and 0-2 cyclopenthy moieties (Fig. S2 online) [18]. The utility in temperature reconstructions is based on the capacity of bacteria to alter the fluidity of their lipid membrane to adjust to colder conditions by producing more methyl branches, and vice versa [18]. Because of the consistent variations between lake-surface and air temperatures [19-20] and the relatively weak seasonality in low-latitude areas [21-23], lacustrine brGDGTs-based indices have been proposed as proxies for low-latitude mean annual air temperature (MAAT) reconstructions [23-24]. Meanwhile, Long-chain (C_{27}, C_{29}, C_{31}) *n*-alkanes preserved in lake sediment derive mainly from leaf-wax lipids of terrestrial plants [25-26]. Many studies have demonstrated that leaf-wax δD (δD_{wax}, the weighted average δD values of C_{27}-, C_{29}- and C_{31}-alkanes) can be used to record isotopes of rainfall [27-29]. Specifically, in the Indian monsoon region, leaf-wax δD values have been be used to record isotopes of Indian monsoon rainfall [27, 30-32]. The primary control on rainfall isotopes in the Indian monsoon region is the integrated summer monsoon rainfall between tropical ocean sources and the specific study site through Rayleigh distillation, with lower

114 δD_{wax} values indicating increased rainfall and stronger summer monsoon intensity,
115 and vice versa [33-34]. As both δD_{wax} and high-precision U-series dated Chinese
116 speleothem $\delta^{18}O$ records reflect water isotope fractionation processes in the same
117 monsoon rainfall [33-34], and are similarly affected by processes in the hydrological
118 cycle [35], analyzing brGDGTs and leaf wax δD from a single lake sediment core
119 could not only help to constrain the age model of lake sediments beyond the time
120 coverage of the radiocarbon dating method, but also help to identify the potential
121 orbital-scale difference in seasonality between annual temperature and summer
122 monsoon intensity over the last glacial stage.

123 In addition, paleoclimate models can infer the driving force behind reconstructed
124 climate changes. TraCE 21ka (TraCE) is the first state-of-art transient simulation of
125 the global climate over the period of the last 21 ka using fully coupled NCAR
126 CCSM3 with T31 spatial resolution (3.75°x3.75°) [36], forced by realistic climatic
127 forcings that comprise orbital insolation [37], atmospheric GHG [38], meltwater
128 discharge/AMOC changes [39], and continental ice sheets (ICE-5G) [40].
129 Modifications of coastlines and bathymetry are performed at 13.1, 12.9, 7.6 and 6.2
130 ka for the Barents Sea, the Bering Strait, Hudson Bay, and the Indonesian
131 throughflow, respectively [41-42]. In spite of the limitation of insufficient knowledge
132 about meltwater discharge from continental ice sheets, TRACE 21ka has been found
133 to reproduce paleoclimatic variations in considerable detail through parallel
134 sensitivity experiments across climate change events [41-42]. Simulations include
135 both the general climate transition from the glacial to interglacial state [10, 43], and
136 the main climate change events such as H1, BA, YD during the last deglacial [42, 44-
137 45].

In this study, we report both brGDGTs and δD_{wax} records over the past 88,000 years, inferred from exactly the same sample set of a lake sediment core collected in Hengduan Mountains, southwestern China (Fig. S1 online). Together with the advanced TraCE climate simulations, we aim to (1) reconstruct both MAAT and summer monsoon intensity variations since the last glacial stage at a terrestrial site in Indian monsoon-influenced southern Asia; (2) identify the potential orbital-scale seasonal difference between annual temperature and hydroclimate in this region; (3) infer the driving mechanism behind obtained paleoclimate changes; (4) provide a more reliable paleoclimate background for the living conditions of anatomically modern humans.

2 Materials and methods

2.1 Study site

Both Lake Tengchongqinghai (25°07′ N, 98°34′E; 1885m asl) and Lugu Lake (27°41'N, 100°45'E; 2685 m a.s.l.) are located in the Hengduan Mountains at the southeastern margin of the Tibetan Plateau (Fig. S1 online), within the influence of the Indian summer monsoon [46]. Lake Tengchongqinghai is close to the Yushuping Archaeology Site, where anatomically modern humans lived at around 30 ka [47] (Fig. S1 online). Lake Tengchongqinghai is a small freshwater crater (maar) lake with a surface area of ~0.25 km^2 and a catchment area of ~1.5 km^2. The mean water depth is ~5.2 m, and the maximum water depth is ~8.1 m. The closed lake is mainly recharged by direct precipitation, groundwater, and surface runoff from the catchment basin, with no visible outlet. Lugu Lake is a tectonically formed alpine freshwater lake with a surface area of ~50 km^2 and a catchment area of 171.4 km^2. The mean

water depth is ~40 m, and the maximum water depth is ~94 m. The lake resides within an inter-montane basin that is fed mainly by direct precipitation and surface runoff, along with two very small inflowing rivers in the south (Sanjiacun River and Shankua River). The lake is drained via Caohai wetland in the southeast into Gaizu River, a tributary of the Yangtze River [48].

2.2 Sample collection

In 2017, a 2237-cm long sediment core (TCQH17A), reaching the bedrock of the lake bottom, was drilled at ~6 m water depth from the center of Lake Tengchongqinghai using a mechanical platform sampling system. After initial descriptions in the laboratory, sediment cores were sliced at 2-cm intervals. In this study, a total of ~290 subsamples were selected and analyzed for brGDGTs and leaf-wax hydrogen isotope analyses. In 2010, an 860-cm-long core (LG10) was drilled at ~70 m water depth in the center of Lugu Lake using a UWITEC sampling system [48]. After initial descriptions in the laboratory, sediment cores were sliced at 1-cm intervals. In this study, we focus on the top ~500 cm for brGDGTs analyses to obtain Holocene MAAT record, with a total of ~190 subsamples. We have also collected 20 modern sediment samples from 9 lakes in southwestern China, spanning a large elevational range between ~1500 and ~4000 m a.s.l. and thus a temperature range between ~2 and ~18 °C (Table. S1). In addition, 11 and 8 soil samples have been collected from the catchments of Lugu Lake and Lake Tengchongqinghai, respectively.

2.3 Age model

Construction of the chronology for core TCQH17A involves two steps. First, we obtained 13 AMS-^{14}C dates from the top 10 meters of the core (going back to 35 ka),

mostly from terrestrial plant fragments (Fig. S3 online and Table. S2 online). The resulting ^{14}C dates were calibrated to calendar ages using IntCal13 calibration curves [49] (Table. S2) in the program CLAM2.2 [50]. Second, based on the almost identical variations in our δD_{wax} record and the speleothem record [4], we correlated our δD_{wax} record for the section below 10 meter with the Chinese speleothem $\delta^{18}O$ records from Hulu, Dongge, and Sanbao Caves, which had been dated previously using the high-precision radiometric U-series dating technique [4], by finding 6 anchor points through graphically correlation of both time series using *Analyseries* [51] (Fig. S3 online). We checked the resulted interval at 88-35 ka with that from the speleothem $\delta^{18}O$ timeseries, using the 'cross-correlation' function in the program. That yields a peak correlation (r=0.7) under their current phase relation of both time series.

The 95% uncertainty of each anchor point is conservatively considered from plus/minus the time span of 2 sampling points of our δD_{wax} analyses. With the top of core TCQH17A setting as -66 year before present (equivalent to the year 2016) because of the well-preserved water-sediment surface, an age model was then developed using linear interpolation method with the CLAM 2.2 code in the software "R". We contend that our age model is robust, based on the observation that both our δD_{wax} and Chinese speleothem $\delta^{18}O$ records show almost identical variations (Fig. S3 online), and the fact that both isotope proxies share the same physical control mechanisms and come from water isotopes in monsoon rainfall.

The age model for core LG10 is transferred from parallel core LG08, which has a chronology based on 13 AMS-^{14}C dates measured on 5 samples of terrestrial plant remains and 8 of bulk organic matter [48]. An old-carbon effect of ^{14}C age 1662±214 year was determined and corrected for regarding bulk organic samples

[48]. The resulting 13 ^{14}C dates were calibrated to calendar ages and then an age model was constructed through linear interpolation [48].

2.4 Organic geochemical analysis

Freeze-dried subsamples were ultrasonically agitated in organic solvents (dichloromethane:methanol =9:1, v/v) for lipid extraction. After saponification of extracted lipids by 6% potassium hydroxide in methanol solution, the neutral lipids were extracted with *n*-hexane, and then separated into apolar (containing *n*-alkanes) and polar fractions (containing GDGTs) with silica gel (100% activated) column chromatography, using *n*-hexane and methanol, respectively [52]. The polar fractions were filtered through a 0.45 μm PTFE polytetrafluoroethylene filter before analysis. The following analyses were performed in the State Key Laboratory of Biogeology and Environmental Geology, China University of Geosciences.

Compound specific hydrogen isotope ratios of *n*-alkanes were measured by a Delta-V advantage Isotope Ratio Mass Spectrometer (IRMS, Thermo Finnigan) connected to a Gas Chromatography (GC) Ultra^{TM} trace (Thermo Finnigan). Apolar fractions containing approximately 300 ng *n*-alkanes were injected into the GC with a splitless mode, with the injector temperature of 290 °C. The GC oven temperature program was 50 °C (held 1 min) to 210 °C at 10 °C/min (held 2 min), then to 300 °C at 6 °C/min, and finally ramped to 310 °C at 10 °C/min (held 25 min). The *n*-alkanes were converted to hydrogen gas using a high-temperature pyrolysis reactor at 1,400°C, and then their hydrogen isotopes were measured by the IRMS. During all the experiments, the H_3^+ factor varied between 3.7 and 4.2 during the sample analysis and daily variation <0.1 [53]. The stability of the IRMS was checked with an *n*-alkane mixture (n-C_{23}, n-C_{25}, n-C_{27}, n-C_{29}, and n-C_{31} alkane) and the Indiana A4 mixture

with known δ^2H values between every two samples. Squalane (δ^2H value: -167‰) was used as the internal standard. Standard deviation for hydrogen isotope analysis was less than ±5‰, based on at least duplicate analyses. Results are reported in the delta notation (‰) relative to the Vienna Standard Mean Ocean Water standard (VSMOW). The down-core δD results from C_{27}, C_{29}, and C_{31} –alkanes are shown in Fig. S4 online.

Identification and quantification of brGDGTs were performed using Agilent 1200 series liquid chromatograph linked to a triple quadrupole mass spectrometer (LC-MS2) system, equipped with auto-injection mode and Masshunter qualitative software. The polar fractions were spiked with an aliquot of internal C_{46} standard and re-dissolved in 300 μL solvents (*n*-hexane:ethyl acetate, EtOA, 84:16, v/v) with injection volume of 10 μL. Separation of 5- and 6-methyl brGDGTs isomers was achieved with two Silica columns in tandem (each 150 mm× 2.1 mm, 1.9 μm, Thermo Finnigan; USA), maintained at 40 °C. The elution gradients of GDGTs were *n*-hexane:EtOA solvent (84:16, v/v) for the first 5 min, followed by a linear gradient change to n-hexane:EtOA solvent (82:18, v/v) from 5 to 65 min and then to 100% EtOA for 21 min, followed by 100% EtOA for 4 min to wash the column and then back to n-hexane:EtOA solvent (84:16, v/v) to equilibrate the column. The constant flow rate was 0.2 ml/min throughout. The MS conditions were: nebulizer pressure 60 psi, vaporizer temperature 400°C, drying gas flow rate 6 L/min and temperature 200°C, capillary voltage 3500 V, corona 5 μA. Selected ion monitoring (SIM) was used, monitoring at m/z 1050, 1048, 1046, 1036, 1034, 1032, 1022, 1020, 1018 for the regular of brGDGTs. Quantification of GDGTs was achieved by using an external standard and integrating peaks areas of the $[M+H]^+$ ions, assuming an identical

response factor for GDGTs. The 5- and 6-methyl brGDGTs were assigned as described in [54].

2.5 brGDGT data analyses, MAAT reconstruction and uncertainty assessment

We calculate fractional abundances of summed tetra-, penta-and hexa-methylated brGDGTs of the 20 modern samples from the 9 lakes in southwestern China, down-core samples from both core LG10 and core TCQH17A, and modern soil samples from both lake catchments. We also compare with results of modern samples from East African lakes [24] and global soils [55] (Fig. S5 online). All these results derive from the new brGDGT analytical method, with separation of 5-methyl and 6-methyl isomers.

We choose recently proposed Index1 [55] as the proxy for mean annual air temperature (MAAT) reconstructions, which is also one of the recommended calibrations for East African lakes [24]. To fully propagate the uncertainties of the calibration and our temperature reconstructions, we performed a linear ordinary least-squares regression of Index 1 against MAAT, yielding a calibration line and its 2σ confidence interval (Fig. S6a online). The predictive ability of our model and the uncertainty in our reconstruction were evaluated by bootstrapping, which generated 5000 replicates assumed to mimic the actual distribution of the model parameters (Fig. S6b, c online). The bootstrapped coefficient of determination (R^2) and root mean squared error of prediction (RMSEP) are 0.91 and 2.49, respectively. Uncertainties of MAAT time-series were calculated from the bootstrapping and expressed in terms of 95% confidence interval.

3 Results and discussion

3.1 Evaluation and validation of MAAT reconstruction

The results from both modern and down-core lake sediments in southwestern China are consistent with those from East African Lakes (Fig. S5a, c online). Results from soils in both lake catchments are also consistent with those from global soils (Fig. S5b, d online). This suggests that brGDGT distributions in southwestern China follow closely the global or broader-scale lacustrine/soil brGDGT patterns with separation of 5-methyl and 6-methyl isomers (Fig. S5 online).

However, brGDGT distributions between soils and lake sediments (both down-core and modern samples) are distinct in either Lugu or Tengchongqinghai catchments. At Lugu Lake, for example, fractional abundances of hexa- (0.3-0.46) and tetra-methylated (0.11-0.18) brGDGTs in lake sediments have ranges that are distinct from those in catchment soils (0.02-0.2 for hexa- and 0.19-0.62 for tetra-) (Fig. S5a, b online). While at Lake Tengchongqinghai, fractional abundances of penta- (0.3-0.5) and tetra-methylated (0.3-0.6) brGDGTs in lake sediments also have ranges that are distinct from those in catchment soils (0-0.3 for penta- and 0.7-0.9 for tetra-) (Fig. S5c, d online). Although we cannot completely exclude any brGDGT contribution from soils based only on these differences, our comparison still suggests that brGDGT sources in both lakes are dominated by autogenic lacustrine origins rather than soil contributions in both modern and downcore sediments.

Considering the broadly similar environmental variables and climatic background of both lake groups (Table. S1), and the similar brGDGT-MAAT calibration functions based on East African lakes (MAAT=12.22+18.79*Index1, R^2=0.92) and SW Chinese lakes (MAAT=11.08+20.69 *Index1, R^2=0.84), it is reasonable to combine the results

from both lake groups to obtain a more reliable function (MAAT=12.18+19.11*Index1, R^2=0.92, RMSE=2.49 °C) for our study area (Fig. S6a online). Also, study of brGDGTs in African lakes has demonstrated that MAAT explains the majority of the variations in the East African lake brGDGT data (by comparing with other variables such as lake depth, surface and bottom pH, conductivity, surface area, surface and bottom dissolved oxygen, etc.), and that the inferred MAAT calibrations may be appropriate in tropical lakes outside East Africa [24]. With all our downcore brGDGTs falling within range of these modern lake sediments, the calibration is robust for reconstructing low-latitude MAAT changes for this study.

We compare the Index1-based and traditional MBT'$_{5ME}$-based MAAT reconstructions (Fig. S7 online), and find the Index1-based calibration can get a more realistic MAAT at Lake Tengchongqinghai which is comparable to instrumental data, although both time series vary consistently. For instance, the reconstructed core-top temperature of ~17.9 °C agrees well (within its 2-sigma uncertainties) with the modern mean annual temperature of 17.5 °C at the year 2016 obtained from the nearby Baoshan Meteorological Station. We further validate the Holocene MAAT of Lake Tengchongqinghai with another reconstruction from the nearby higher-elevation, larger Lugu Lake, using exactly the same method based on the Index1. Both records show a similar overall trend in the Holocene, but the Lugu record shows less high-frequency variability and more similarity to the TraCE model output (Fig. S7-S8 online). In addition, another brGDGT-inferred MAAT record from Lake Tengchongqinghai [56], re-calculated by our new calibration function, shows an overall similar pattern with ours during the past 50 ka (Fig. S7a online).

In addition, we calculate the Branched Isoprenoid Tetraether index (BIT) and

CBT'-derived pH records for both lakes, although the recent study shows that brGDGT-derived lake pH values have larger uncertainties [24]. In core TCQH17A from Lake Tengchongqinghai, BIT values fall in a quite small range (0.97 to 1) relative to many other lakes (Fig. S7 online), which indicates a rather stable microbial populations over the past ~88 kyr. At orbital scales, there are small changes (up to 0.03) in BIT values which show some similarities with variations of our δD_{wax}-derived monsoon intensities (Fig. S7 online), indicating that orbital-scale BIT changes have been probably driven by monsoon rainfall rather than MAAT. Similarly, orbital-scale changes in inferred pH values also show similarities with changes in our monsoon intensity record (Fig. S7 online). In addition, lithology of the core, although without distinct lithofacies variations, still shows subtle changes consistent with orbital-scale monsoon variations (Fig. S3 online). These findings suggest that our inferred MAAT changes are independent from other environmental variables at Lake Tengchongqinghai.

At Lugu Lake, the inferred downcore pH values do not show a clear correlation with our reconstructed MAAT data either (Fig. S8 online). Calculated downcore BIT values are relatively stable at ~0.9 before 10 ka and then decreased to ~0.6 during over the past 10 ka (Fig. S8 online). Although BIT values in the Holocene section are roughly anti-phased with our MAAT data, they do not show an obvious change during the last deglaciation when the MAAT experienced a temperature drop at 13-12 ka (the Younger Dryas event) and then a warming trend at 12-10 ka. Similar to Lake Tengchongqinghai, therefore, brGDGT-inferred MAAT in Lugu Lake does not seem to be substantially influenced by other environmental variables, as was also indicated in modern East African lakes [24]. In addition, the MAAT record at Lugu

354 Lake shows a consistent change with that from TraCE simulations, further supporting
355 the reliability of this MAAT record (Fig. S7-S8 online).

356 3.2 Reconstructed MAAT variations in southwestern China

357 Our MAAT record from Lake Tengchongqinghai shows pronounced orbital-
358 scale periodic warm intervals since the last glaciation, including an ~2.5 °C warming
359 interval from 88 to 71 ka, an up to ~2 °C warmer period from 45 to 22 ka, and a
360 progressive ~3 °C warming from the end of the last glacial maximum around 19 ka to
361 the late Holocene (Fig. 1c). During the intercalated colder intervals, MAAT values
362 averaged about 14-15 °C (Fig. 1c). The inferred temperature difference of ~3°C
363 between means for the last glacial maximum and Holocene agrees with previous
364 estimates of 2-4°C for low-latitude oceans [57] and many low-elevation sites in
365 tropical terrestrial regions [58-59].

366 The pattern of temporal variability in our reconstructed MAAT record differs
367 markedly from that of Asian summer monsoon intensity records, including our own
368 δD_{wax} record from the same sample set and the absolute-dated Chinese speleothem
369 $\delta^{18}O$ records [4] (Fig. 1a-c). In particular, our MAAT data do not show the ~23,000-
370 year precession cycle, which is especially prominent in the summer monsoon-
371 intensity records from Chinese caves (Fig. 1a-c). The cave records are strongly
372 affected by hydroclimate variations throughout low-latitude summer monsoon areas
373 [4], which is corroborated by the agreement with our δD_{wax} record. Summer
374 monsoons were intense during Marine Isotope Stage 5a (MIS5a) and weak during
375 MIS 4. Conversely, our MAAT reconstruction shows that the warm period lagged
376 peak summer monsoon intensities in MIS 5a as recorded by δD_{wax} from the same set
377 sample. Moreover, the warm period extended from MIS 5a into early MIS 4 (Fig. 1a-

c). During MIS 3, summer monsoon intensities were relatively high, but MAAT was low throughout the first half of this interval (Fig. 1a-c). Summer monsoon intensities were low during MIS 2, while a warm period revealed by our MAAT data spanned the later stage of MIS 3 and early MIS 2 until 22 ka (Fig. 1a-c). During the Holocene, summer monsoon intensity decreased, whereas MAAT continued to increase since the last glacial maximum (Fig. 1a-c).

Our MAAT record also differs substantially from global-scale and many regional temperature reconstructions obtained from marine sediments, polar ice cores, and Chinese loess sections. Atmospheric CO_2 concentrations [60] (Fig. 1e), high-latitude temperatures from Antarctic [61] (Fig. 1f) and Greenland ice cores [62], and global mean SST [63] all display an overall declining trend during the last glacial stage, typical of the so-called "saw-tooth"-shaped ~100,000-year global glacial-interglacial cycle. Summer-biased temperature records derived from soil brGDGTs from the mid-latitude Chinese Loess Plateau, where the brGDGT producer organisms are sensitive to moisture availability in this semi-arid region and probably experience optimum growth during East Asian summer monsoon season [64-65], also show this glacial-interglacial pattern [64-66], although some display strong ~23,000-year precessional cycles similar to those characteristics of summer monsoon intensities [65]. In contrast, our Lake Tengchongqinghai MAAT shows two long warm intervals in the cold last glacial stage, which reach amplitudes close to the full glacial-interglacial range (Fig. 1c). Conversely polar and global temperatures, and atmospheric CO_2 levels, were relatively high in the period centered on 55 ka (Fig. 1e, f), while our Tengchongqinghai MAAT stayed low (Fig. 1c).

A classic "saw-tooth"-shaped global glacial-interglacial cycle has also been reported for many low-latitude SST reconstructions [6-8]. However, some more

proximal low-latitude SST records from the western Arabian Sea [67], Bay of Bengal [68], and northern Arabian Sea [69] seem more consistent with our MAAT record (Fig. S9 online). We infer that the driver of annual mean temperature variations in southwestern China, and - at least - in the aforementioned northern sectors of the Indian Ocean, was fundamentally different from the driver of summer monsoon intensity and that of the global temperature, which is strongly influenced by northern high-latitude climate.

During the Holocene, our MAAT data show an overall warming trend, which contrasts with the cooling trend in stacked records of global annual temperature [11-12]. Within low latitudes, most available Holocene temperature records, including SSTs and terrestrial temperatures, derive from locations outside of the Indian monsoon-influenced southern Asia [11]. These data usually show contrasting annual temperature trends at different areas, including both warming and cooling in the Indo-Pacific Warm Pool [70-71], the Indian Ocean [72-73], and tropical Africa [74]. This indicates the existence of major spatial heterogeneity in low-latitude Holocene annual temperature trend. Within Indian-monsoon influenced terrestrial regions, available Holocene temperature records concern summer temperatures in southwestern China [13-14], which show a cooling trend through the Holocene that contrasts with the warming trend in our MAAT record (Fig. 2). This difference between summer-specific and annual mean temperatures in southwestern China highlights the critical importance of understanding seasonality in Indian-monsoon influenced terrestrial temperature reconstructions. In the following, we disentangle the different drivers on our MAAT record using TraCE simulations [45].

3.3 Driving force of Holocene temperature changes in southern Asia

The two MAAT records from Lake Tengchongqinghai and Lugu Lake show similar overall trends and amplitudes of change (Fig. 2a, b), indicating our data can capture regional temperature pattern in southwestern China. Then, we compare both MAAT records with the TraCE simulations [45]. Model-simulated MAAT records under all forcings for the study region show strong similarity with our two MAAT reconstructions, with respect to both the general trend and the amplitudes of overall changes (Fig. 2a, b). A bit discrepancy likely exists over the late Holocene. Our MAAT records also show a temperature decrease at that time (Fig. 2a), which agrees with a recent temperature reconstruction for North America and Europe [75], but which is not apparent in TraCE simulations (Fig. 2a-b). We suggest that this may reflect a lack of influences of volcanic and solar-variability [76], as well as anthropogenic forcing in the TraCE simulations, which certainly needs to be tested with additional paleoclimate data and models in the future.

Regarding the overall trend of annual mean temperatures, TraCE simulations with individual forcings reveal that the deglacial warming in our record is mainly forced by GHG increase, while Holocene warming is mainly forced by increasing low-latitude annual mean insolation with an additional GHG contribution after 6 ka, with very limited influences of ice-sheet and melt-water changes (Fig. S10 online). Although a general Holocene warming in low latitudes are evident in TraCE and other simulations [15], an obvious spatial heterogeneity also exists (Fig. 3). In these models, the warming Holocene pattern with strong sensitivity to annual insolation is coherent throughout tropical northern Africa (~10-20 °N), the southern Arabia Peninsula, India, and southwestern China, which cover our study site (Fig. 3b) (see also ref [15]). Beyond these regions, the influence of annual mean insolation is

451 relatively weak (Fig. 3b) (see also ref [15]), and this is unfortunately where most
452 available low-latitude records derive from [11]. Notably, some local factors could
453 override the effect of annual insolation, and induce substantial spatial heterogeneity in
454 Holocene annual temperature trends. For instance, Holocene SST discrepancies in the
455 Indo-Pacific Warm Pool and Indian Ocean may be attributed to monsoon-induced
456 ocean circulation patterns [71-72], influences of northern high-latitude climates [70]
457 and/or seasonal bias in SST proxies [73, 77], while Holocene temperature changes in
458 tropical and southern Africa have been linked to a complex interplay of local annual
459 maximum insolation [78], tropical hydrology [79], southwestern Indian Ocean SST
460 [80], and northern high-latitude climates [81-82]. Fortunately, model simulations
461 suggest that our study site is in the less-complicated region where local annual
462 insolation influences are dominant (Fig. 3b) (see also ref [15]). Regarding summer
463 temperatures, both reconstructions (Fig. 2c) and TraCE output (Fig. S10 online)
464 indicate an overall decreasing trend through the Holocene for southwestern China,
465 which is strongly related to local (boreal) summer insolation (Fig. 2c and Fig. S10
466 online). This summer temperature trend contrasts markedly with our observed and
467 simulated warming trend through the Holocene in annual mean temperatures, which
468 relate to annual mean insolation (Fig. 2a, b and Fig. S10 online).

469 While we find good agreement between the TraCE simulation records and our
470 observed annual mean temperature reconstructions for southwestern China, TraCE
471 (and other models) also suggest a global mean Holocene warming trend, driven by
472 declining high-latitude ice sheets and slightly increasing atmospheric CO_2
473 concentrations [16]. This contrasts with global-mean proxy-based paleotemperature
474 syntheses, which suggest a global-mean annual-mean cooling through the Holocene
475 [11-12]. This discrepancy has been attributed to the summer bias in many

paleotemperature records [16, 75, 83], and especially in those from northern mid- and high-latitude regions where most records in the global compilations come from [11-12, 15]. In addition, a recent synthesis of model simulations infers that this discrepancy can be related to Arctic amplification and sea ice loss driven by boreal summer insolation, which would cause decreasing Holocene annual mean temperatures in the northern extratropics [15], which are overrepresented in the global-mean proxy-based paleotemperature syntheses. However, all these models consistently show a warming Holocene trend in our study region, with a considerable contribution of local annual mean insolation [15-16]. This is consistent with our new record.

3.4 Possible obliquity-induced warmth in southern Asia during the last glacial stage

Although the TraCE simulation does not extend beyond 21 ka, the identified annual mean insolation and atmospheric GHG (mainly CO_2) concentrations may also work for Lake Tengchongqinghai record at longer timescales. Indeed, the orbital-scale variations in our MAAT record coincide with the timing of changes in both factors within the last glacial stage. From 88 to 71 ka, for instance, the observed ~2.5°C warming in MAAT coincided with rising annual mean insolation along with 20-30 ppm elevated atmospheric CO_2 concentrations from a background value of ~220 ppm. The abrupt ending of this warm period coincides with a sharp CO_2 decline of ~40 ppm, along with decreasing annual mean insolation. From 45 to 22 ka, increased annual mean insolation in the region of Lake Tengchongqinghai alone, without CO_2 increase, sufficed to increase annual mean temperature by about ~2°C. During the last deglaciation, ~3°C warming occurred in response to a rapid CO_2 increase of ~80 ppm, despite an overall decline of annual mean insolation.

In order to better evaluate the influence of local annual insolation and GHG on our MAAT record, we make a simple estimation by combing these two radiative forcings after measuring both of them in W/m^2 (conversion of GHG forcing after ref [84], which include both CO_2 and CH_4), albeit they have different wavelengths (Fig. 1d). The calculated result suggests this combined radiative forcing is basically consistent with our MAAT record during the past ~90 ka (Fig. 1d). The three peaks at 88-71 ka, 45-22 ka and 14-0 ka correspond well with the three warm periods in our MAAT record (Fig. 1d). However, the combined forcing decreased gradually at 71-60 ka and reached its lowest value around 45 ka, while our MAAT reached its lowest value at the entire 71-45 ka interval (Fig. 1d). This mismatch may be largely due to the simplicity of the estimation method for radiative forcings, which does not take into account many additional processes such as atmospheric-oceanic circulations and land covers, which could amplify these radiative forcings and induce large changes. Also, the calculated insolation is at the top of the atmosphere rather than the Earth surface, which likely overestimates the forcing at the land surface. In addition, other trace gases such as N_2O will increase the GHG radiative forcing as well. Together with these uncertainties, we speculate those additional processes could be spatial- and time-variable, which certainly needs to be further studied with a data and model synthesis in the future.

It is probably that the identified warm periods at 88-71 ka and 45-22 ka in our MAAT record were mainly induced by local annual mean insolation. The rise and fall of low-latitude annual mean insolation is strongly regulated by the ~41,000-year cycle of obliquity or tilt of Earth's axis relative to its orbital plane (Fig. 1f), which exerts opposite annual mean insolation effects in high and low latitudes, with the switch-over centered on 40-45° latitude [17, 84]. Decreased obliquity reduces annual mean

525 insolation in high-latitude regions, but increases annual mean insolation in low-
526 latitude regions [17, 84]; this was the case during the warm intervals at 88-71 ka and
527 45-22 ka recorded in our MAAT record. Compared with the relatively small
528 amplitudes of this effect during the Holocene, the much larger increase in low-latitude
529 annual mean insolation during the 88-71 ka and 45-22 ka intervals could override the
530 influence of northern high-latitude climate and other possible localized factors, and
531 may cause warmer conditions over some larger areas, such as the northern reaches of
532 the Indian Ocean (Fig. S9 online). Our compilation and new data may reveal
533 pervasive and widespread impacts of obliquity-induced annual mean insolation
534 changes in the low latitudes, particularly in Southern Asia. This influence is
535 recognized even in the Holocene, when obliquity impacts were relatively small (Fig.
536 1f). However, we notice many other paleoclimate records, although from the
537 simulated annual-insolation sensitive regions such as low-latitude Africa, show some
538 contrasting temperature changes [74] and inconsistent with our record [74, 85].
539 Therefore, our finding and model simulations need to be assessed with additional
540 temperature records from low-latitude land and ocean sites with excellent chronology,
541 high sampling resolutions, and preferably with clear distinction of seasonal signals.

542 **4 Conclusions and implications**

543 We present the first, highly-resolved record of annual mean temperature in
544 Indian-monsoon influenced Southern Asia that covers the entire last glacial cycle. It
545 demonstrates that orbital-scale changes in annual mean temperature were decoupled
546 from summer monsoon fluctuations in the region. In particular, we recognize two key
547 intervals (88-71 ka and 45-22 ka) of elevated annual mean temperature that are close
548 to the full glacial-interglacial range. With the output of TraCE simulations and
549 comparing with forcing factors, we find these warm periods are probably forced by

local annual mean insolation and secondarily GHGs, while the monsoon intensity tends to be closely associated with season-specific summer insolation.

Our findings may offer new insight into the living conditions of anatomically modern humans in Asia, providing our observed annual-insolation-induced MAAT changes also works in broader areas as suggested by TraCE and other models [15]. The two warm intervals within the last glacial stage coincide with intervals of highest frequencies of dated evidence [1] for anatomically modern humans in Asia (Fig. 1c, g). While monsoon records (Fig. 1a, b) also show generally high summer monsoon intensities in these warm intervals, the interval 61-45 ka has high monsoon intensities but low frequencies of dated archaeological evidence. This suggests that the grouping of archaeological datings is more consistent with the occurrence of our warm intervals (or warmth plus active monsoons), rather than with active monsoons alone. Thus, our new temperature record may highlight the importance of temperature for anatomically modern humans in these regions within the last glacial stage.

Acknowledgments

We thank the editors and three anonymous referees for their thoughtful reviews and constructive suggestions. We thank L. Yang for organic geochemical pretreatments, X. Huang, H. Yang, J. Li, and S. Gao for brGDGTs analyses and hydrogen isotope analyses. We thank J.W. Williams, H. Wu, H. Lu for helpful discussions. This research is supported by the Strategic Priority Research Program of Chinese Academy of Sciences (#XDB 40000000 & # XDA2009000004), the Program of Global Change and Mitigation, Ministry of Science and Technology of the

573 People's Republic of China (#2016YFA0600502), and National Natural Science
574 Foundation of China (#41877293 & 41472315).

575 **Author contributions**

576 C. Z. and J.S. designed the study. C. Z., X. Y., E. Zhang collected sediment
577 cores. Z.L. and J. C. performed climate simulations and analyses. X. F., X. S., C.
578 Zhang, and T. Y. performed lab work and data analyses. S.Y performed statistical
579 analyses. C.Z. and E.J.R. led writing the paper. All authors contributed to discussion
580 the results and writing of the manuscript.

581 **Conflict of interest**

582 Authors declare no competing financial interests.

583 **Data and materials availability**

584 All data is available in the main text or the supplementary materials.

585

586 **References**

587 1. Bae CJ, Douka K, Petraglia MD (2017) On the origin of modern humans: Asian
588 perspectives. *Science* 358, eaai9067.

589 2. Timmermann A, Friedrich T (2016) Late Pleistocene climate drivers of early
590 human migration. *Nature* 538: 92-95.

591 3. Beck JW, Zhou W, Li C et al (2018) A 550,000-year record of East Asian monsoon
592 rainfall from ^{10}Be in loess. *Science* 360, 877-881.

593 4. Cheng H, Edwards RL, Sinha A et al (2016) The Asian monsoon over the past
594 640,000 years and ice age terminations. *Nature* 534, 640-646.

595 5. An Z, Steven CC, Shen J et al (2011) Glacial-interglacial Indian summer monsoon
596 dynamics. *Science* 333, 719-723.

597 6. Herbert TD, Peterson LC, Lawrence KT et al (2010) Tropical ocean temperatures
598 over the past 3.5 million years. *Science* 328, 1530-1534.

599 7. Oppo DW, Sun Y (2005) Amplitude and timing of sea-surface temperature change
600 in the northern South China Sea: Dynamic link to the East Asian monsoon. *Geology*
601 33, 785-788.

602 8. Saraswat R, Nigam R, Weldeab D et al (2005) A first look at past sea surface
603 temperatures in the equatorial Indian Ocean from Mg/Ca in foraminifera. *Geophys.*
604 *Res. Lett.* 32, L24605.

605 9. Shakun JD, Clark PU, He F et al (2012) Global warming preceded by increasing
606 carbon dioxide concentrations during the last deglaciation. *Nature* 484, 49-54.

607 10. Clark PU, Shakun JD, Baker PA et al (2012) Global climate evolution during the
608 last deglaciation. *Proc. Natl. Acad. Sci. U.S.A.* 109, 1134-1142.

609 11. Kaufmann D, McKay N, Routson C et al (2020) A global database of Holocene
610 paleotemperature records. *Sci. Data* 7, 115.

611 12. Marcott SA, Shakun JD, Clark PU et al (2013) A reconstruction of regional and
612 global temperature for the past 11,300 years. *Science* 339, 1198–1201.

613 13. Wu D, Chen X, Lv F et al (2018) Decoupled early Holocene summer temperature
614 and monsoon precipitation in southwest China. *Quat. Sci. Rev.* 193, 54-67.

615 14. Zhang E, Chang J, Cao Y et al (2018) Holocene high-resolution quantitative
616 summer temperature reconstruction based on subfossil chironomids from the
617 southeast margin of the Qinghai-Tibetan Plateau. *Quat. Sci. Rev.* 165, 1-12.

618 15. Park HS, Kim SJ, Stewart AL et al (2019) Mid-Holocene Northern Hemisphere
619 warming driven by Arctic amplification. *Sci. Adv.* 5, eaax8203.

620 16. Liu Z, Zhu J, Rosenthal Y et al (2014) The Holocene temperature conundrum.
621 *Proc. Natl. Acad. Sci. U.S.A.* 111, 3501-3505.

622 17. Laskar J, Robutel P, Joutel F et al (2004) A long term numerical solution for the
623 insolation quantities of the Earth. *Astron Astrophys.* 428, 261-285.

624 18. Weijers JWH, Schouten S, van den Donker JC et al (2007) Environmental
625 controls on bacterial tetraether membrane lipid distribution in soils. *Geochim.*
626 *Cosmochim. Acta* 71, 703–713.

627 19. Loomis SE, Russell JM, Heureux AM et al (2014) Seasonal variability of
628 branched glycerol dialkyl glycerol tetraethers (brGDGTs) in a temperate lake system.
629 *Geochim. Cosmochim. Acta* 144, 173–187.

630 20. Livingstone DM, Lotter AF (1998) The relationship between air and water
631 temperatures in lakes of the Swiss Plateau: a case study with palæolimnological
632 implications. *J. Paleolimnol*. 19, 181-198.

633 21. Shanahan TM, Hughen KA, Van Mooy BAS (2013) Temperature sensitivity of
634 branched and isoprenoid GDGTs in Arctic lakes. *Org. Geochem.* 64, 119-128.

635 22. Loomis SE, Russell JM, Ladd B et al (2012) Calibration and application of the
636 branched GDGT temperature proxy on East African lake sediments. *Earth Planet.*
637 *Sci. Lett.* 357, 277-288.

638 23. Tierney JE, Russell JM, Eggermont H et al (2010) Environmental controls on
639 branched tetraether lipid distributions in tropical East African lake sediments.
640 *Geochim. Cosmochim. Acta* 74, 4902-4918

641 24. Russell JM, Hopmans EC, Loomis SE et al (2018) Distributions of 5- and 6-
642 methyl branched glycerol dialkyl glycerol tetraethers (brGDGTs) in east African lake
643 sediment: effects of temperature, pH, and new lacustrine paleotemperature
644 calibrations. *Org. Geochem*. 117, 56-69.

645 25. Cranwell PA, Eglinton G, Robinson N (1987) Lipids of aquatic organisms as
646 potential contributors to lacustrine sediments–II. Org. Geochem. 11, 513–527.

647 26. Eglinton G, Hamilton RJ (1967). Leaf epicuticular waxes. Science 156, 1322–
648 1335.

649 27. Contreras-Rosales LA, Jennerjahn T, Tharammal T et al (2014) Evolution of the
650 Indian Summer Monsoon and terrestrial vegetation in the Bengal region during the
651 past 18 ka. *Quat. Sci. Rev*. 102, 133-148.

652 28. Tipple BJ, Pagani M (2013) Environmental control on eastern broadleaf forest
653 species' leaf wax distributions and D/H ratios. *Geochim. Cosmochim. Acta*. 111, 64–
654 77.

655 29. Sachse D, Billault I, Bowen GJ et al (2012) Molecular Paleohydrology:
656 Interpreting the Hydrogen-Isotopic Composition of Lipid Biomarkers from
657 Photosynthesizing Organisms. Annu. Rev. *Earth Pl. Sc.* 40, 221–249.

658 30. Wang C, Hren MT, Hoke GD et al (2017) Soil *n*-alkane δD and glycerol dialkyl
659 glycerol tetraether (GDGT) distributions along an altitudinal transect from southwest

660 China: Evaluating organic molecular proxies for paleoclimate and paleoelevation.
661 *Org. Geochem.* 107, 21–32.

662 31. Jia G, Wei K, Chen F (2008) Soil *n*-alkane δD vs. altitude gradients along Mount
663 Gongga, China. *Geochim. Cosmochim. Acta.* 72, 5165–5174.

664 32. Mügler I, Sachse D, Werner M et al (2008) Effect of lake evaporation on δD
665 values of lacustrine *n*-alkanes: a comparison of Nam Co (Tibetan Plateau) and
666 Holzmaar (Germany). *Org. Geochem.* 39, 711– 729.

667 33. Liu Z, Wen X, Brady EC et al (2014) Chinese cave records and the East Asia
668 Summer Monsoon. *Quat. Sci. Rev.* 83, 115-128.

669 34. Pausata FSR, Battisti DS, Nisancioglu KH et al (2011) Chinese stalagmite $\delta^{18}O$
670 controlled by changes in the Indian monsoon during a simulated Heinrich event. *Nat.*
671 *Geosci.* 4, 474–480.

672 35. Hoefs J (1996) Stable isotope geochemistry: fourth completely revised, updated,
673 and enlarged edition. Springer-Verlag, Berlin, pp 201.

674 36. Collins WD, Bitz CM, Blackmon ML et al (2006) The community climate system
675 model version 3 (CCSM3). *J. Clim.* 19, 2122–2143.

676 37. Berger A (1978) Long-term variations of daily insolation and quaternary climatic
677 changes. *J. Atmos. Sci.* 35, 2362–2367.

678 38. Joos F, Spahni R (2008) Rates of change in natural and anthropogenic radiative
679 forcing over the past 20,000 years. *Proc. Natl. Acad. Sci. U.S.A.* 105, 1425–1430.

680 39. McManus JF, Francols R, Gherardi JM et al (2004) Collapse and rapid resumption
681 of Atlantic meridional circulation linked to deglacial climate changes. *Nature* 428,
682 834-837.

683 40. Peltier W (2004) Global glacial isostasy and the surface of the ice-age earth: the
684 ICE-5G (VM2) model and GRACE. *Annu. Rev. Earth Pl. Sc.* 32, 111–149.

685 41. He F (2011) Simulating Transient Climate Evolution of the Last Deglaciation with
686 CCSM3. Dissertation, University of Wisconsin-Madison, USA.

687 42. Liu Z, Carlson AE, He F et al (2012) Younger Dryas cooling and the Greenland
688 climate response to CO_2. *Proc. Natl Acad. Sci. U.S.A.* 109, 11101–11104.

689 43. He F, Shakun JD, Clark PU et al (2013) Northern Hemisphere forcing of Southern
690 Hemisphere Climate during the last deglaciation. *Nature* 494, 81–85.

691 44. Otto-Bliesner BL, Russell JM, Clark PU et al (2014) Coherent changes of
692 southeastern equatorial and northern African rainfall during the last deglaciation.
693 *Science* 346, 1223–1227.

694 45. Liu Z, Otto-Bliesner BL, He F et al (2009) Transient simulation of Last
695 Deglaciation with a new mechanism for Bolling-Allerod warming. *Science* 325, 310–
696 314.

697 46. Yao T, Masson-Delmotte V, Gao J et al (2013) A review of climatic controls on
698 $\delta^{18}O$ in precipitation over the Tibetan Plateau: observations and simulations. *Rev.*
699 *Geophys.* 51, 525-548.

700 47. Liu HG (2016) Human activities and agriculture resources utilization from
701 Paleolithic to Bronze Age in northwest Yunnan province. Dissertation, Lanzhou
702 University, Lanzhou (in Chinese).

703 48. Wang Q, Yang X, Anderson NJ et al (2016) Direct versus indirect climate
704 controls on Holocene diatom assemblages in a sub-tropical deep, alpine lake (Lugu
705 Hu, Yunnan, SW China). *Quat. Res.* 86, 1-12.

706 49. Reimer PJ, Bard E, Bayliss A et al (2013) IntCal13 and Marine13 radiocarbon age
707 calibration curves, 0-50,000 years cal BP. *Radiocarbon* 55: 1869-1887.

708 50. Blaauw M (2010) Methods and code for 'classical' age-modelling of radiocarbon
709 sequences. *Quat. Geochron*. 5: 512-518.

710 51. Paillard D (1996) Macintosh Program performs time-series analysis. *Eos*
711 *Transactions, American Geophysical Union* 77, 39.

712 52. Feng X, Zhao C, D'Andrea WJ et al (2019) Temperature fluctuations during the
713 Common Era in subtropical southwestern China inferred from brGDGTs in a remote
714 alpine lake. *Earth Planet. Sci. Lett.* 510, 26-36.

715 53. Zhao B, Zhang Y, Huang X et al (2018) Comparison of *n*-alkane molecular,
716 carbon and hydrogen isotope compositions of different types of plants in the Dajiuhu
717 peatland, central China. *Org. Geochem.* 124, 1–11.

718 54. De Jonge C, Hopmans EC, Stadnitskaia A et al (2013) Identification of novel
719 penta- and hexamethylated brached glycerol dialkyl glycerol tetraethers in peat using
720 HPLC–MS2, GC–MS and GC–SMB-MS. *Org. Geochem.* 54, 78–82.

721 55. De Jonge C, Hopmans EC, Zell CI et al (2014) Occurrence and abundance of 6-
722 methyl branched glycerol dialkyl glycerol tetraethers in soils: Implications for
723 palaeoclimate reconstruction. *Geochim. Cosmochim. Acta 141*, 97–112.

724 56. Tian L, Wang M, Zhang X et al (2019) Synchronous change of temperature and
725 moisture over the past 50 ka in subtropical southwest China as indicated by biomarker
726 records in a crater lake. *Quat. Sci. Rev.* 212, 121-134.

727 57. Mohtadi M, Prange M, Oppo DW et al (2014) North Atlantic forcing of tropical
728 Indian Ocean Climate. *Nature* 509, 76-80.

729 58. Loomis SE, Russell JM, Verschuren D et al (2017) The tropical lapse rate
730 steepened during the Last Glacial Maximum. *Sci. Adv*. 3, e1600815.

731 59. Mark BG, Harrison SP, Spessa A et al (2005) Tropical snowline changes at the
732 last glacial maximum: A global assessment. *Quat. Int*. 138-139, 168-201.

733 60. Bereiter B, Eggleston S, Schmitt J et al (2015) Revision of the EPICA Dome C
734 CO_2 record from 800 to 600 kyr before present. *Geophys. Res. Lett.* 42, 542–549.

735 61. Petit JR, Jouzel J, Raynaud D et al (1999) Climate and atmospheric history of the
736 past 420,000 years from the Vostok ice core, Antarctica. *Nature* 399, 429-436.

737 62. NGRIP members (2004) High-resolution record of Northern Hemisphere climate
738 extending into the last interglacial period. *Nature* 431, 147-151.

739 63. Friedrich T, Timmermann A, Tigchelaar M et al (2016) Nonlinear climate
740 sensitivity and its implications for future greenhouse warming. *Sci. Adv.* 2, e1501923.

741 64. Lu H, Liu W, Yang H et al (2019) 800-kyr land temperature variations modulated
742 by vegetation changes on Chinese Loess Plateau. *Nat. Commun.* 10, 1958.

743 65. Peterse F, Martinez-Garcia A, Zhou B et al (2014) Molecular records of
744 continental air temperature and monsoon precipitation variability in East Asia
745 spanning the past 130,000 years. *Quat. Sci. Rev.* 83, 76-82.

746 66. Gao L, Niu JS, Clemens S et al (2012) The importance of solar insolation on the
747 temperature variations for the past 110 kyr on the Chinese Loess Plateau.
748 *Palaeogeogr. Palaeoclimatol. Palaeoecol.* 317-318, 128–133.

749 67. Rostek F, Bard E, Beaufort L et al (1997) Sea surface temperature and
750 productivity records for the past 240kyr in the Arabian Sea. *Deep-sea Research II* 44,
751 1461-1480.

752 68. Raza T, Ahmad SM, Steinke S et al (2017) Glacial to Holocene changes in sea
753 surface temperature and seawater $\delta^{18}O$ in the northern Indian Ocean. *Palaeogeogr.*
754 *Palaeoclimatol. Palaeoecol.* 485, 697–705.

755 69. Schulte S, Muller PJ (2001) Variations of sea surface temperature and primary
756 productivity during Heinrich and Dansgaard-Oeschger events in the northeastern
757 Arabian Sea. *Geo-Marine Letters* 21, 168-175.

758 70. Zhang Y, Zhu K, Huang C et al (2019) Asian winter monsoon imprint on
759 Holocene SST changes at the northern coast of the South China Sea. *Geophys. Res.*
760 *Lett.* 46, 13363-13370.

761 71. Moffa-Sanchez P, Rosenthal Y, Babila TL et al (2019) Temperature evolution of
762 the Indo-Pacific Warm Pool over the Holocene and the last deglaciation. *Paleocean.*
763 *Paloclimatol.* 34, 1107-1123.

764 72. Boll A, Schulz H, Munz P et al (2015) Contrasting sea surface temperature of
765 summer and winter monsoon variability in the northern Arabian Sea over the last 25
766 ka. *Palaeogeogr. Palaeoclimatol. Palaeoecol.* 426, 10–21.

767 73. Huguet C, Kim JH, Sinninghe Damste JS et al (2006) Reconstruction of sea
768 surface temperature variations in the Arabian Sea over the last 23 kyr using organic
769 proxies TEX_{86} and $U_{37}^{K'}$. *Paleoceanography* 21, PA3003.

770 74. Berke MA, Johnson TC, Werne JP et al (2012) Molecular records of climate
771 variability and vegetation response since the Late Pleistocene in the Lake Victoria
772 basin, East Africa. *Quat. Sci. Rev.* 55, 59-74.

773 75. Marsicek J, Shuman BN, Bartlein PJ et al (2018) Reconciling divergent trends and
774 millennial variations in Holocene temperatures. *Nature* 552, 92-96.

775 76. Bader J, Jungclaus J, Krivova N et al (2020) Global temperature mode shed light
776 on the Holocene temperature conundrum. *Nat. Commun.* 11, 4726.

777 77. Leduc G, Schneider R, Kim JH et al (2010) Holocene and Eemian sea surface
778 temperature trends as revealed by alkenone and Mg/Ca paleothermometry. *Quat. Sci.*
779 *Rev.* 29, 989-1004.

780 78. Berke MA, Johnson TC, Werne JP et al (2012) A mid-Holocene thermal
781 maximum at the end of the African Humid Period. *Earth Planet. Sci. Lett.* 351-352,
782 95-104.

783 79. Loomis SE, Russell JM, Lamb HF (2015) Northeast African temperature
784 variability since the Late Pleistocene. *Palaeogeogr. Palaeoclimatol. Palaeoecol.* 423,
785 80–90.

786 80. Chevalier M, Chase BM (2015) Southeast African records reveal a coherent shift
787 from high- to low-l atitude forcing mechanisms along the east African margin across
788 last glacial-interglacial transition. *Quat. Sci. Rev.* 125, 117-130-74.

789 81. Tiernry JE, Russell JM, Huang Yet al (2008) Northern hemisphere controls on
790 tropical southeast African climate during the past 60,000 years. *Science* 322, 252-255.

791 82. Powers LA, Johnson TC, Werne JP et al (2005) Large temperature variability in
792 the south African tropics since the Last Glacial Maximum. *Geophys. Res. Lett.* 32,
793 L08706.

794 83. Hou J, Li CG, Lee, S (2019) The temperature record of the Holocene: progress
795 and controversies. *Sci. Bull.* 64, 565-566.

84. Rohling EJ, Medina-Elizalde M, Shepherd JG et al (2012) Sea surface and high-latitude temperature sensitivity to radiative forcing of climate over several glacial cycles. *J. Clim* 25, 1635–1656.

85. Castañeda IS, Schouten S, Pätzold J et al (2016) Hydroclimate variability in the Nile River Basin during the past 28,000 years. Earth Planet. Sci. Lett. 438, 47-56.

86. Zhang X, Ha B, Wang S et al (2018) The earliest human occupation of the high-altitude Tibetan Plateau 40 thousand to 30 thousand years ago. *Science* 346, 1049–105.

Figure Captions

Fig. 1. ▏Comparison of the reconstructed annual temperature at Lake Tengchongqinghai and other regional and global paleoclimate reconstructions. (**a**), Speleothem $\delta^{18}O$ data and its 50-point moving averages (thick dark cyan) from Dongge-Hulu-Sanbao Caves in China [4]. VPDB, Vienna Pee Dee belemnite. (**b**), Lake Tengchongqinghai δD_{wax} record (this study) and summer mean isolation (June-July-August) at 30 °N [17]. VSMOW, Vienna Standard Mean Ocean Water. Ticks on top of this panel represents radiocarbon dates (black) and anchor points (blue) between Chinese speleothem $\delta^{18}O$ and Lake Tengchongqinghai δD_{wax} with 2σ errors. (**c**), Lake Tengchongqinghai MAAT record (this study, shaded envelope representing its 2σ uncertainty). The brown tick on the right indicates modern instrumental annual temperature. (**d**), Calculated radiative forcing anomaly based on GHG (including both CO_2 and CH_4, after ref [84]) and annual mean isolation at 30 °N, both forcings are normalized to their own pre-industrial value. (**e**), Atmospheric CO_2 concentrations from the EPICA Dome C [60], and annual mean isolation at 30 °N [17]. (**f**), Reconstructed temperature anomalies inferred from $\delta^{18}O$ values of Vostok ice core in the Antarctic [61] and Earth's obliquity [17]. (**g**), Dating results of archaeology sites of modern humans in low-latitude Asia [1] with 2σ errors, together with two new results from southwestern China and the Tibetan Plateau (Methods and Fig. S1 online). Marine isotope stages are indicated by gray shaded areas, obliquity-forced warm periods are indicated by grayish-yellow shaded areas. The low-CO_2-concentration interval related with the cold period between 71 and 60 ka is highlighted by the light-blue shaded area.

Fig. 2. ┃Comparison of reconstructions and TraCE outputs for annual and summer temperatures in southwestern China. (**a**), Lake Tengchongqinghai MAAT reconstructions with 2σ uncertainty (this study) and TraCE output of Holocene annual mean temperature. (**b**), Lugu Lake MAAT reconstructions with 2σ uncertainty (this study) and TraCE output of Holocene annual mean temperature. (**c**), Tiancai Lake (southwestern China) July temperature reconstructions by chironomids [14] and TraCE output of Holocene summer temperature. All records and TraCE outputs are normalized to their own Holocene mean. TraCE outputs are for our study region in southwestern China, and under full forcing. Results from individual forcing can be found in Fig. S10 online.

Fig. 3. ┃Evaluation of spatial influence of annual-insolation during the Holocene in TraCE. (**a**), Holocene annual temperature tendency (from 10 to 1 ka) under full forcing, which shows that most areas are warming. (**b**), Holocene annual temperature tendency under single orbital forcing, which shows that low latitude areas, including southwestern China, India, Tropical Africa, southern Arabian Peninsula, and eastern Amazonia, are most sensitive to local-annual-insolation forced warming. The black circle in southwestern China indicates our study site.

Cheng Zhao received his Ph.D. degree in Earth and Environmental Sciences from the Department of Earth and Environmental Sciences, Lehigh University (USA) in 2009. After graduation, he worked at the University of Hong Kong and the University of Southampton (UK). Since 2013, he has worked in NIGLAS as a full professor. His research interest includes lake sediments and climate changes, stable and organic geochemistry.

Ji Shen received his bachelor degree from Nanjing University in 1985, and Ph.D. degree from the Department of Geosciences in Nanjing University in 1991. Since then, He has worked in NIGLAS and promoted as a full professor in 1996. In 2020, he joined the School of Geography and Ocean Science in Nanjing University. His research interest focuses on lake sediments and environmental changes.

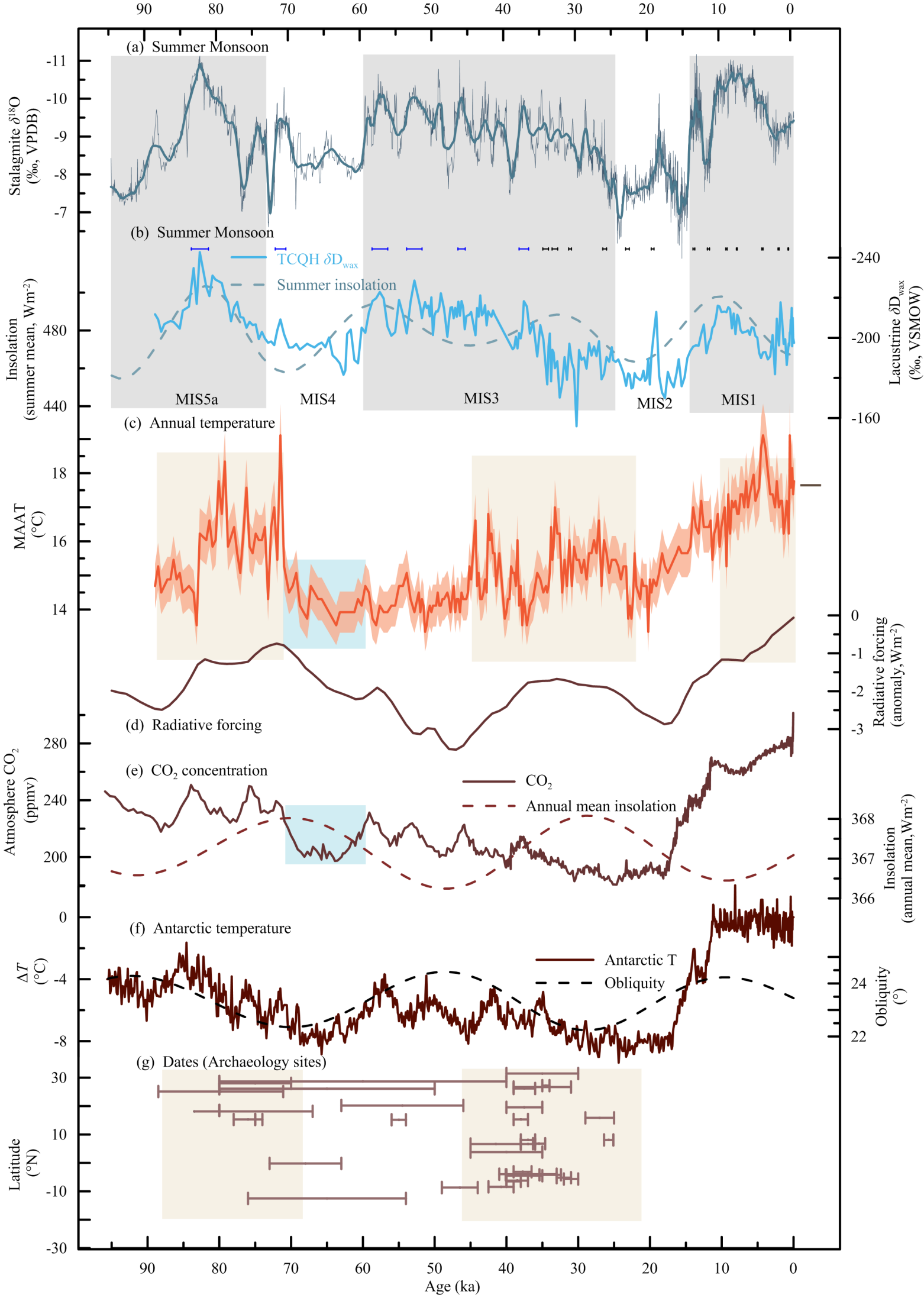
(a) Summer Monsoon
Stalagmite δ18O (‰, VPDB)
-11
-10
-9
-8
-7
(b) Summer Monsoon
TCQH δDwax
Summer insolation
Insolation (summer mean, Wm-2)
480
440
Lacustrine δDwax (‰, VSMOW)
-240
-200
-160
MIS5a
MIS4
MIS3
MIS2
MIS1
(c) Annual temperature
MAAT (°C)
18
16
14
(d) Radiative forcing
Radiative forcing (anomaly, Wm-2)
0
-1
-2
-3
(e) CO2 concentration
CO2
Annual mean insolation
Atmosphere CO2 (ppmv)
280
240
200
Insolation (annual mean, Wm-2)
368
367
366
(f) Antarctic temperature
Antarctic T
Obliquity
ΔT (°C)
0
-4
-8
Obliquity (°)
24
22
(g) Dates (Archaeology sites)
Latitude (°N)
30
10
-10
-30
90
80
70
60
50
40
30
20
10
0
Age (ka)

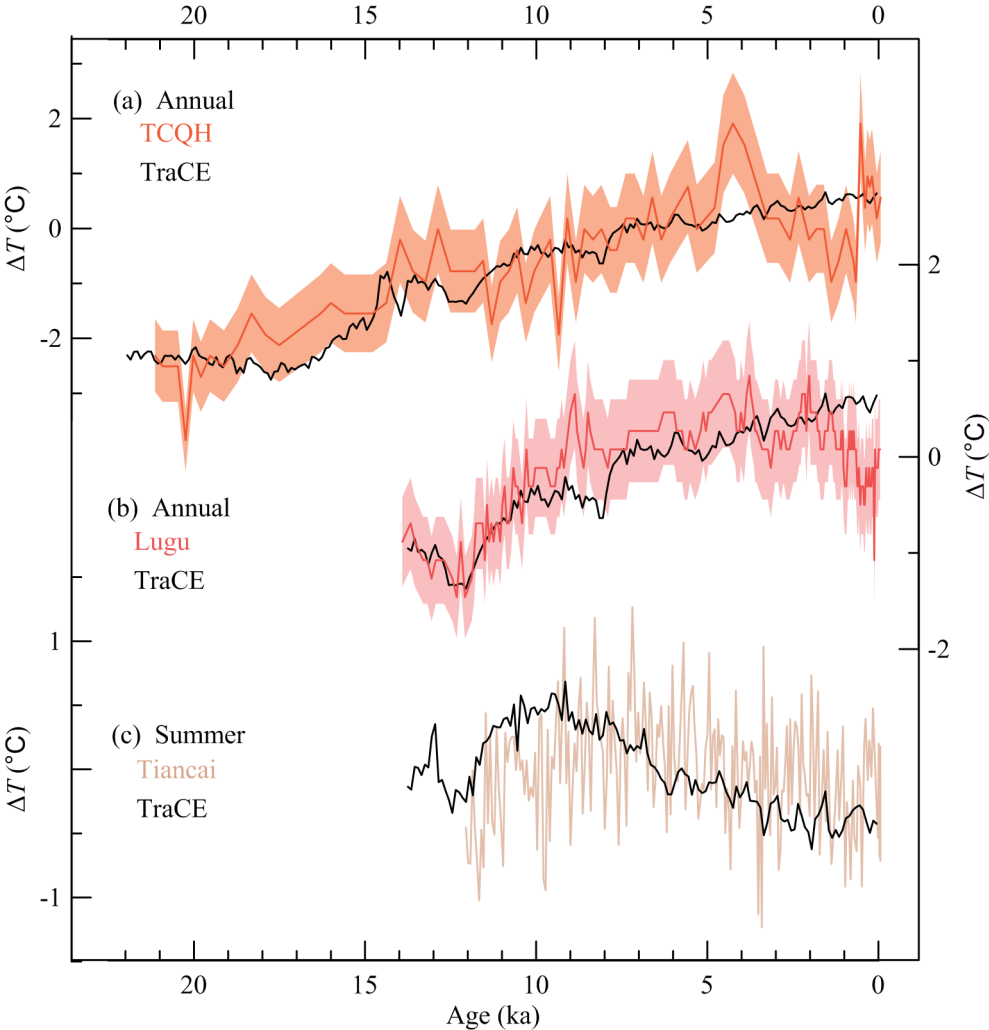
(a) Annual
TCQH
TraCE
(b) Annual
Lugu
TraCE
(c) Summer
Tiancai
TraCE
ΔT (°C)
ΔT (°C)
ΔT (°C)
Age (ka)
20
15
10
5
0
2
0
-2
1
-1

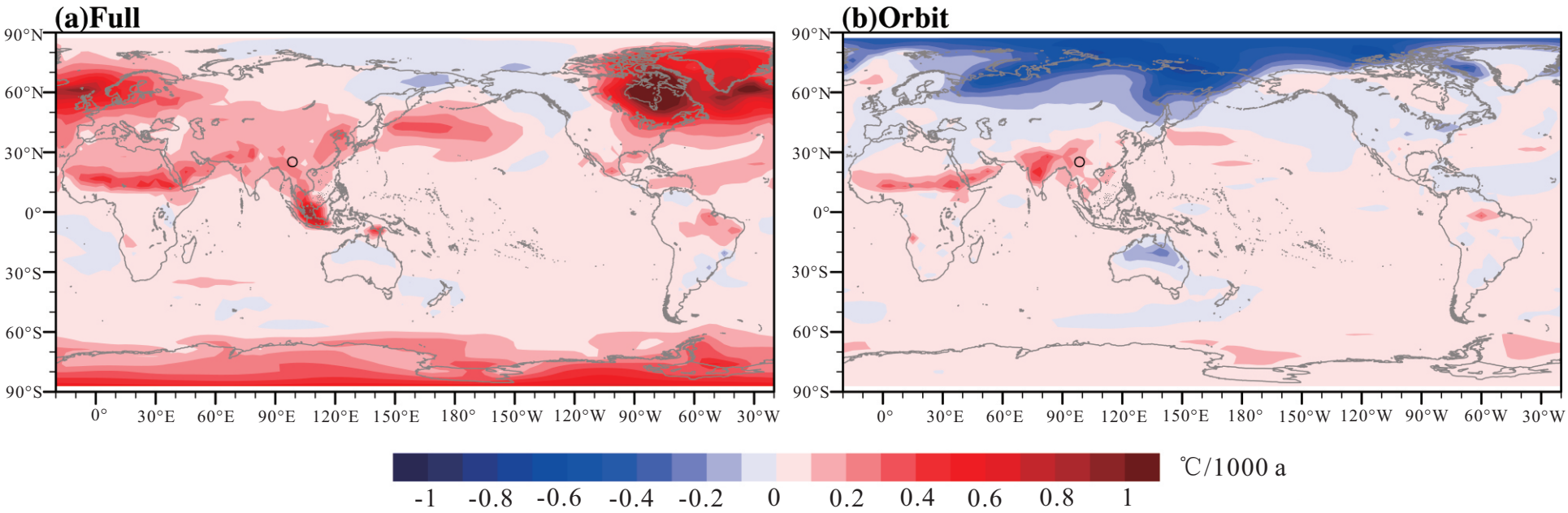
(a)Full
(b)Orbit
90°N
60°N
30°N
0°
30°S
60°S
90°S
0°
30°E
60°E
90°E
120°E
150°E
180°
150°W
120°W
90°W
60°W
30°W
-1
-0.8
-0.6
-0.4
-0.2
0
0.2
0.4
0.6
0.8
1
℃/1000 a

Science Bulletin Manuscript Template
Supplementary Materials

Possible obliquity-forced warmth in southern Asia during the last glacial stage

Cheng Zhao[1,2,3*], Eelco J. Rohling[4,5], Zhengyu Liu[6], Xiaoqiang Yang[7], Enlou Zhang[1,2], Jun Cheng[8], Zhonghui Liu[9], Zhisheng An[2,10], Xiangdong Yang[1], Xiaoping Feng[1], Xiaoshuang Sun[1], Can Zhang[1], Tianlong Yan[1], Hao Long[1,2], Hong Yan[2,10], Zicheng Yu[11,12], Weiguo Liu[2,10], Shi-Yong Yu[13], Ji Shen[1,3*]

[1]State Key Laboratory of Lake Science and Environment, Nanjing Institute of Geography and Limnology, Chinese Academy of Sciences, Nanjing 210008, China.
[2]CAS Center for Excellence in Quaternary Science and Global Change, Xian 710061, China
[3]School of Geography and Ocean Science, Nanjing University, Nanjing 210023, China.
[4]Research School of Earth Sciences, the Australian National University, Canberra ACT 2601, Australia.
[5]Ocean and Earth Science, University of Southampton, National Oceanography Centre, Southampton SO14 3ZH, United Kingdom.
[6]Department of Geography, Ohio State University, 154 N. Oval Mall, Columbus, OH 43210, USA.
[7]Department of Earth Sciences, Sun Yat-Sen University, Guanghzou 510275, China.
[8]Laboratory of Meteorological Disaster, Ministry of Education (KLME)/Joint International Research Laboratory of Climate and Environment Change (ILCEC)/Collaborative Innovation Center on Forecast and Evaluation of Meteorological Disasters (CIC-FEMD), Nanjing University of Information Science and Technology, Nanjing 210044, China.
[9]Department of Earth Sciences, University of Hong Kong, Hong Kong, China.
[10]State Key Laboratory of Loess and Quaternary Geology, Institute of Earth Environment, Chinese Academy of Sciences, Xi'an 710061, China.
[11]Department of Earth and Environmental Sciences, Lehigh University, Bethlehem, Pennsylvania 18015, USA.
[12]Institute for Peat and Mire Research, School of Geographical Sciences, Northeast Normal University, Changchun 130024, China.
[13]School of Geography, Geomatics, and Planning, Jiangsu Normal University, Xuzhou, Jiangsu 221116, China

* Corresponding authors:

Email: czhao@niglas.ac.cn (Cheng Zhao); jishen@niglas.ac.cn (Ji Shen).

This PDF file includes:

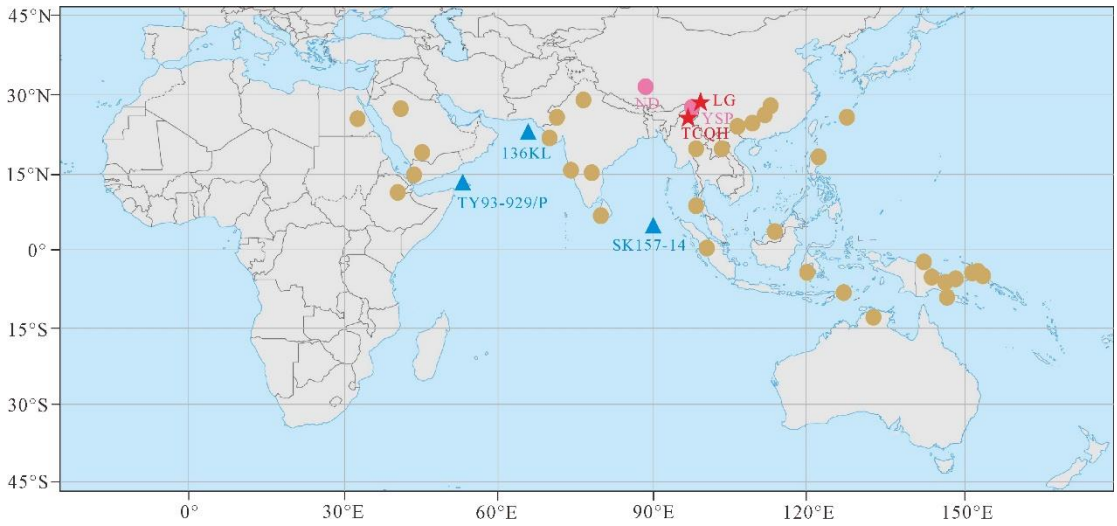

Fig. S1. Overview map of South and East Asia and other related low-latitude areas. The locations of Lake Tengchongqinghai (TCQH) and Lugu Lake (LG) (shown in red stars) are in the Hengduan Mountain in the southeastern Tibetan Plateau, southwestern China. Grayish yellow dots are low-latitude archaeological sites of anatomically modern Homo sapiens during the last glacial time [1], two pink dots are the recently reported Yushuping Site (YSP) in southwestern China [47] and Nwya Deve Site (ND) on the Tibetan Plateau [86]. Blue triangles are locations of SST records with apparent warm intervals during 45-22 ka as mentioned in the text, including core TY93-929/P from the western Arabian Sea [67], core SK157-14 from the Bay of Bengal [68], and core 136KL from the northern Arabian Sea [69].

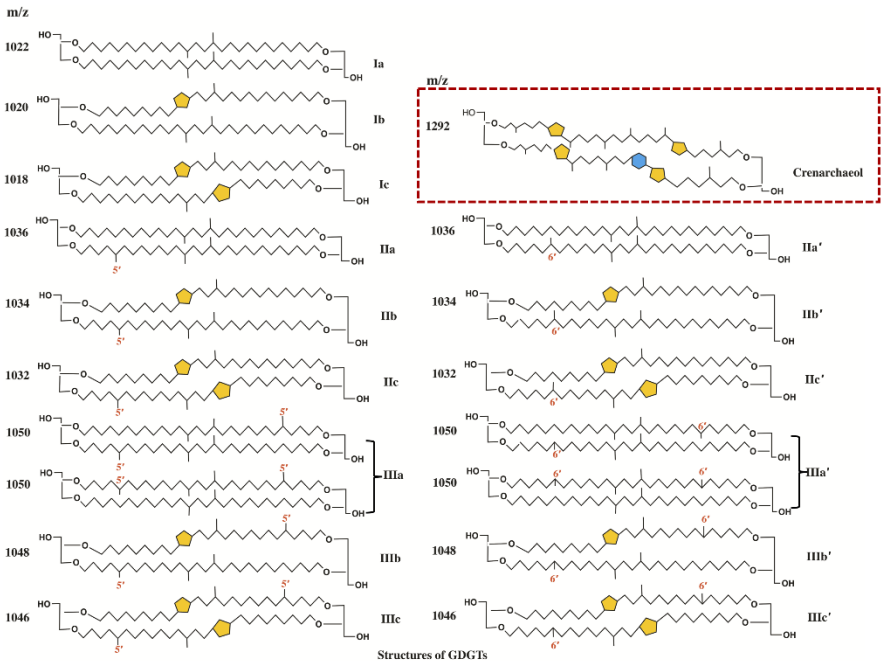

$$MBT'_{5ME}=(Ia + Ib + Ic)/(Ia + Ib + Ic + IIa + IIb + IIc + IIIa)$$

$$Index1= \log[(Ia + Ib + Ic + IIa'+ IIIa')/(Ic + IIa + IIc + IIIa + IIIa')]$$

$$CBT'= -\log[(Ic+ IIa'+ IIb'+ IIc'+ IIIa'+ IIIb'+ IIIc')/(Ia + IIa + IIIa)]$$

$$BIT= (Ia + IIa' + IIa + IIIa + IIIa')/(Ia + IIa' + IIa + IIIa + IIIa'+Crenarchaeol)$$

Fig. S2. brGDGTs and related indices. Structure of individual brGDGT compounds (top) [52] and indices (Index1, MBT'5ME, CBT' and BIT) used for paleo-environmental reconstructions for lake sediments (bottom) [54].

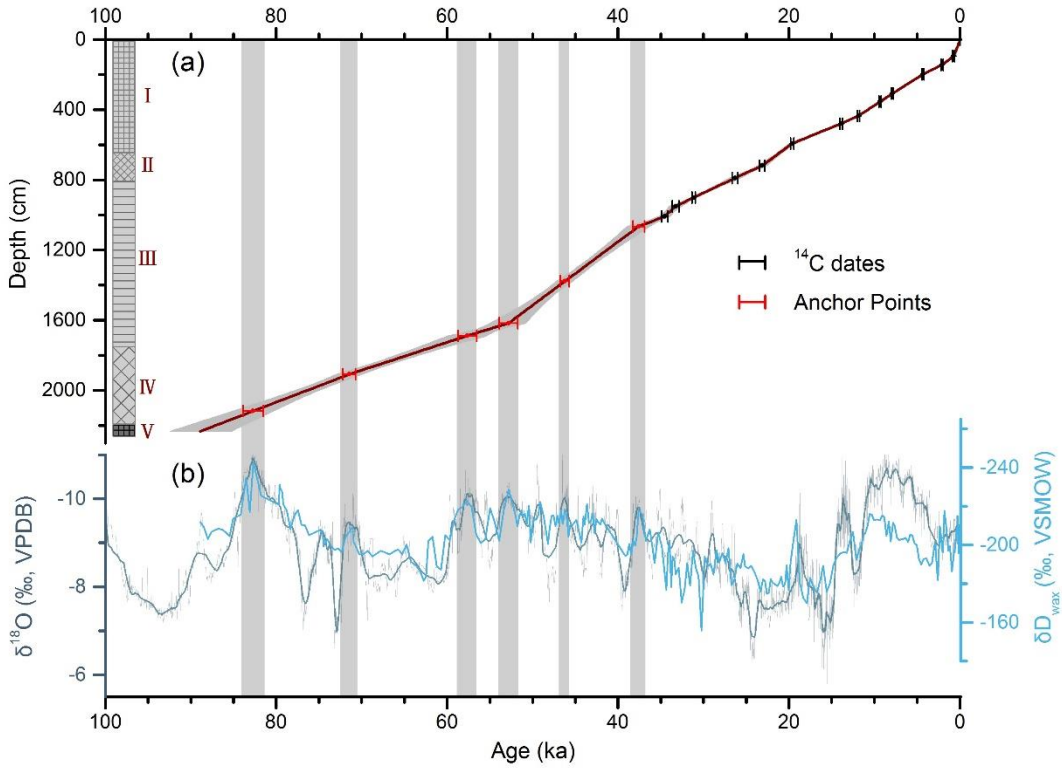

Fig. S3. Age model for core TCQH17A. (**a**), The age model constructed by linear interpolation between each radiocarbon date and correlation anchor (tie) point, with the core top set to -66 year BP. The top 10 meters are constrained by 13 radiocarbon dates, mostly from terrestrial plant fragments (Table. S2). Between 35 and 90 ka, 6 anchor points were constrained by correlation between our δD_{wax} and Chinese speleothem $\delta^{18}O$ records (see **b**). The 2σ uncertainties bounds of each dating and anchor point are indicated with ticks, and with additional gray bars for correlation of anchor points. (**b**), comparison between our δD_{wax} data from Lake Tengchongqinghai (blue) and the Chinese speleothem $\delta^{18}O$ from Dongge-Hulu-Sanbao Caves (gray) [4]. The thick dark cyan line represents 50-point moving averages. The lithology of the core shown in the left of panel a, including I (0-6.57 m): dark gray (brown) massive silty clay to clayey silt; organic rich; II (6.57-7.74 m): gray-black and brown-gray, yellow-brown silty clay; III (7.74-17.55 m): brownish gray, dark gray interbedded silty clay and clayey silt; IV (17.55-21.86 m): brownish gray, dark gray silty clay and clayey silt; V (21.86-22.32 m): dark colored consolidated peat layer.

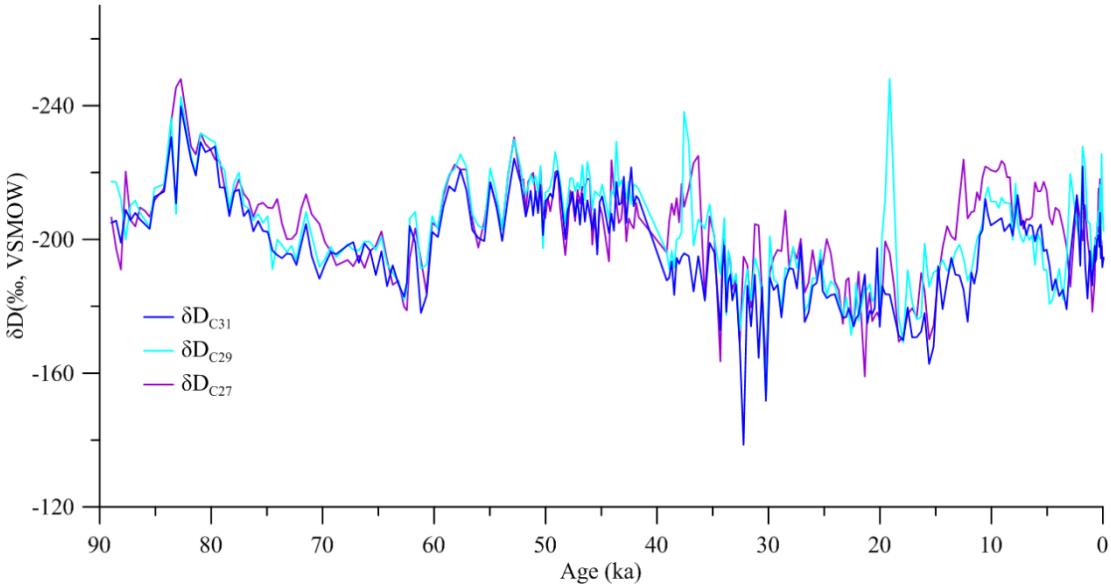

Fig. S4. Comparison of δD data from different long-chain *n*-alkane compounds from core TCQH17A.

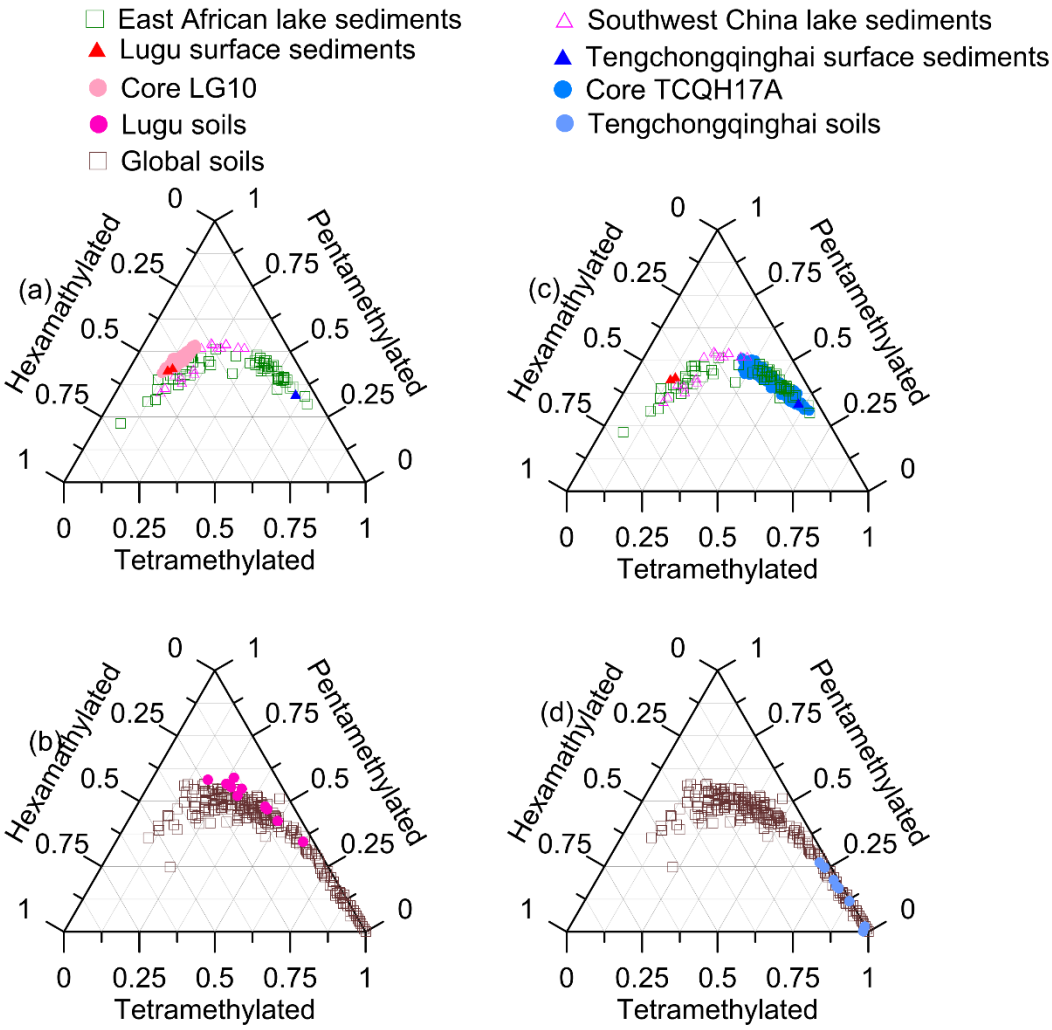

Fig. S5. Comparison of brGDGT distributions in different sample sets. The fractional abundances of summed tetramethylated, pentamethylated, and hexamethylated brGDGTs in lakes (**a**, **c**) and soils (**b**, **d**).

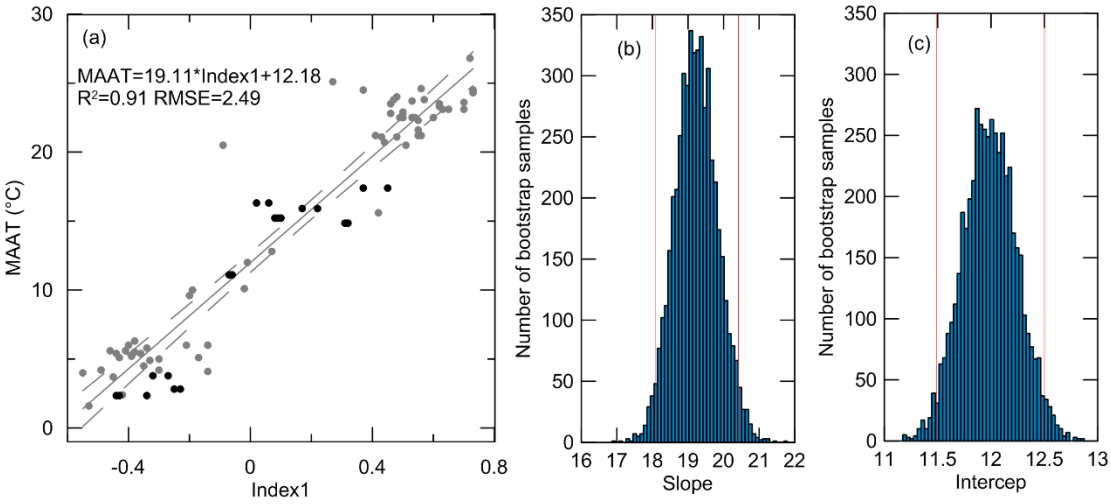

Fig S6. brGDGTs-MAAT calibration and uncertainties. (**a**), Calibration between Index1 and MAAT with 95% confidence limit (2σ error), from 20 modern samples (black dots) collected at 9 lakes in southwestern China (this study) and 65 modern samples (gray dots) collected from African lakes [24]. The gray line is the regression line for all 85 data points. The gray dashed lines indicate the 2σ uncertainty bounds of the regression. (**b**), Histogram showing the frequency distribution of the slope in the linear calibration function. (**c**), Histogram showing the frequency distribution of the intercept in the linear calibration function. Vertical rend lines denote the 95% confidence limit of the parameters.

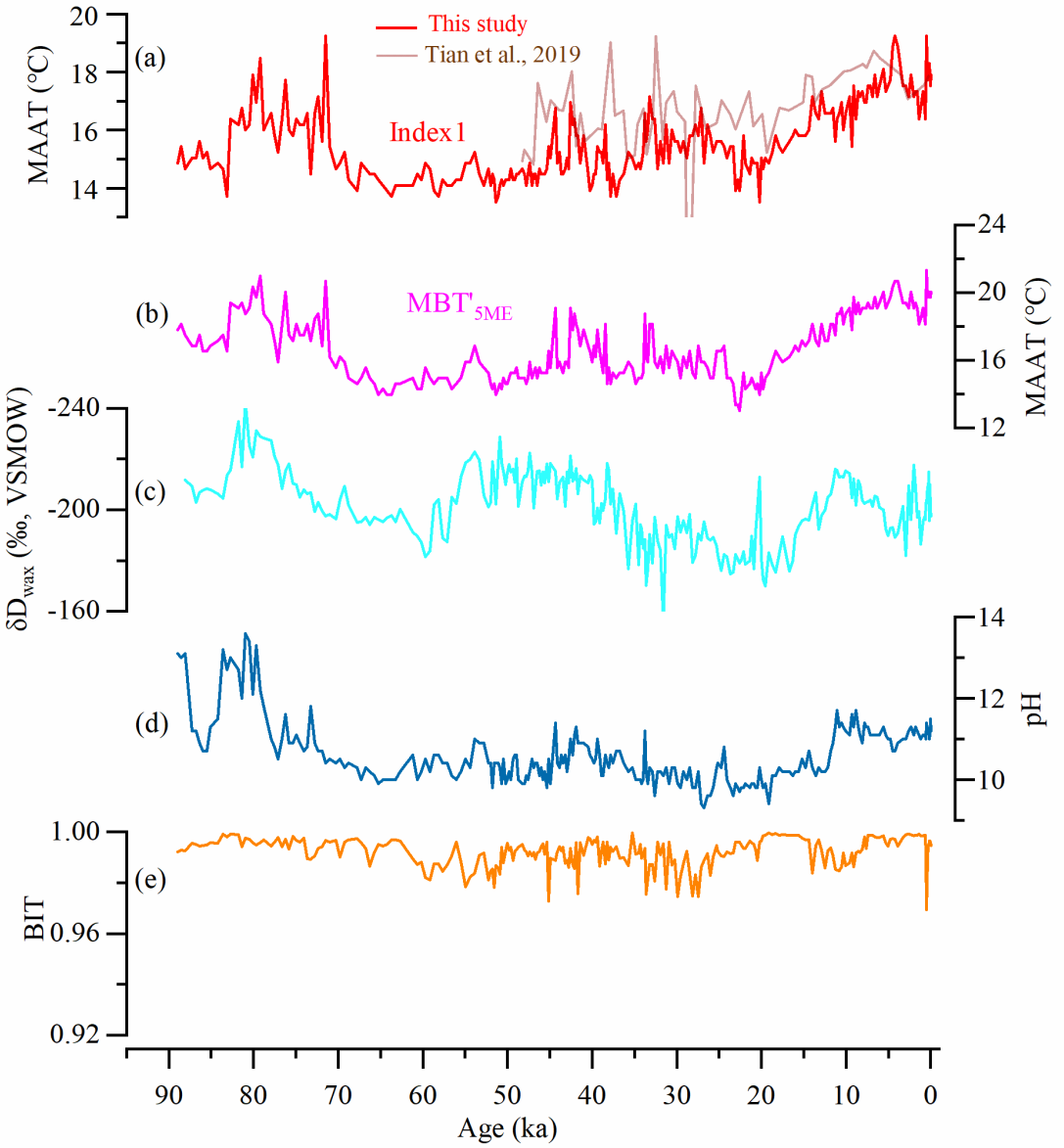

Fig. S7. Downcore variations of brGDGT proxy from core TCQH17A. (**a**), Index1-inferred MAAT, also shown results from another core from the shallow water of Lake Tengchongqinghai [56] calculated by our new transfer function. (**b**), MBT'$_{5ME}$-inferred MAAT. (**c**), δD_{wax}. (**d**), CBT'-inferred pH values [24]. (**e**), calculated BIT values. Both MAAT calibrations are computed based on 20 modern samples from 9 lakes in southwestern China (this study) and 65 modern samples collected from African lakes [24].

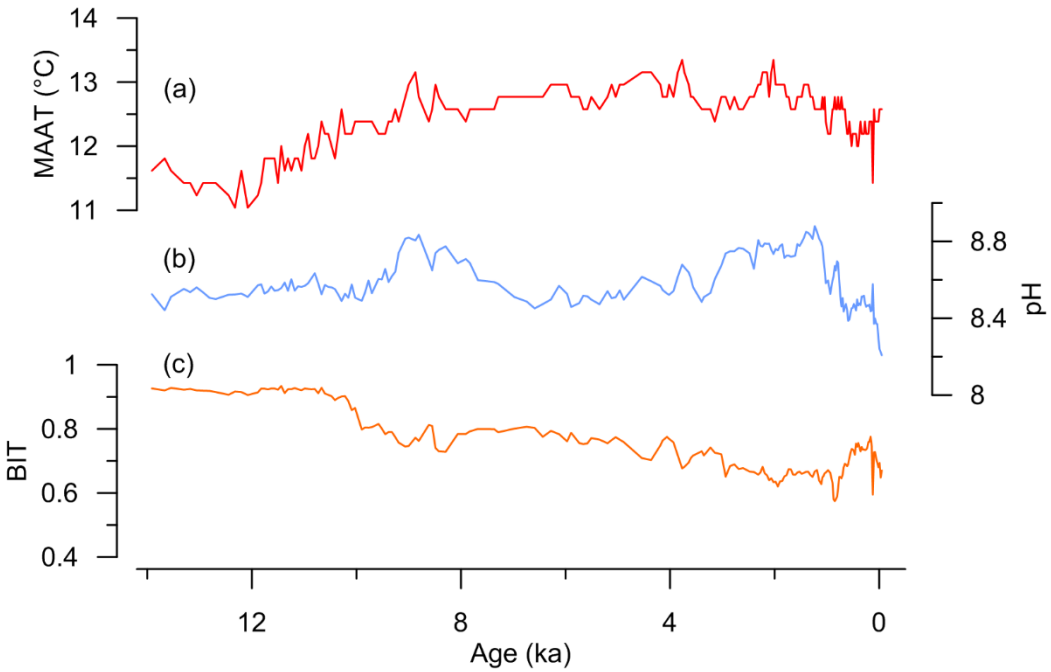

Fig. S8. Downcore variations of brGDGT proxy from core LG10. (**a**), Index1-inferred MAAT. (**b**), CBT'-inferred pH values [24]. (**c**) calculated BIT values. Both MAAT calibrations are computed based on 20 modern samples from 9 lakes in southwestern China (this study) and 65 modern samples collected from African lakes [24].

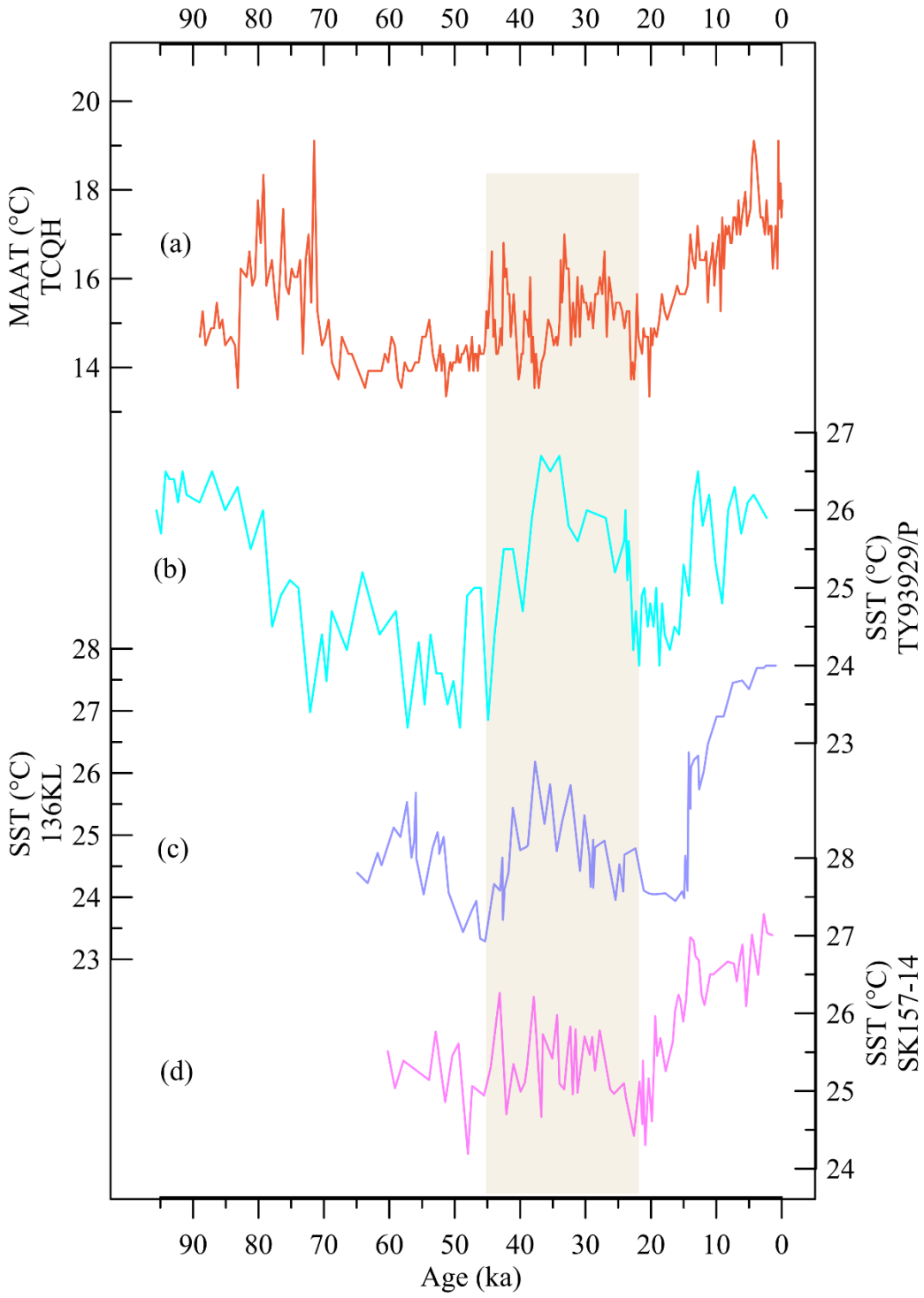

Fig. S9. Comparison of low-latitude land and ocean temperature reconstructions. (**a**), Lake Tengchongqinghai MAAT record. (**b**), $U^{K'}_{37}$ -based SST record from core TY93-929/P in the western Arabian Sea [67]. (**c**), Mg/Ca -based SST record from core 136KL in the northern Arabian Sea [69]. (**d**), Mg/Ca -based SST record from core SK157-14 in the Bay of Bengel [68]. Locations of each record can be found in Fig. S1. The grayish-yellow shaded bands indicate the local annual mean insolation forced warm period from the late MIS 3 and early MIS 2.

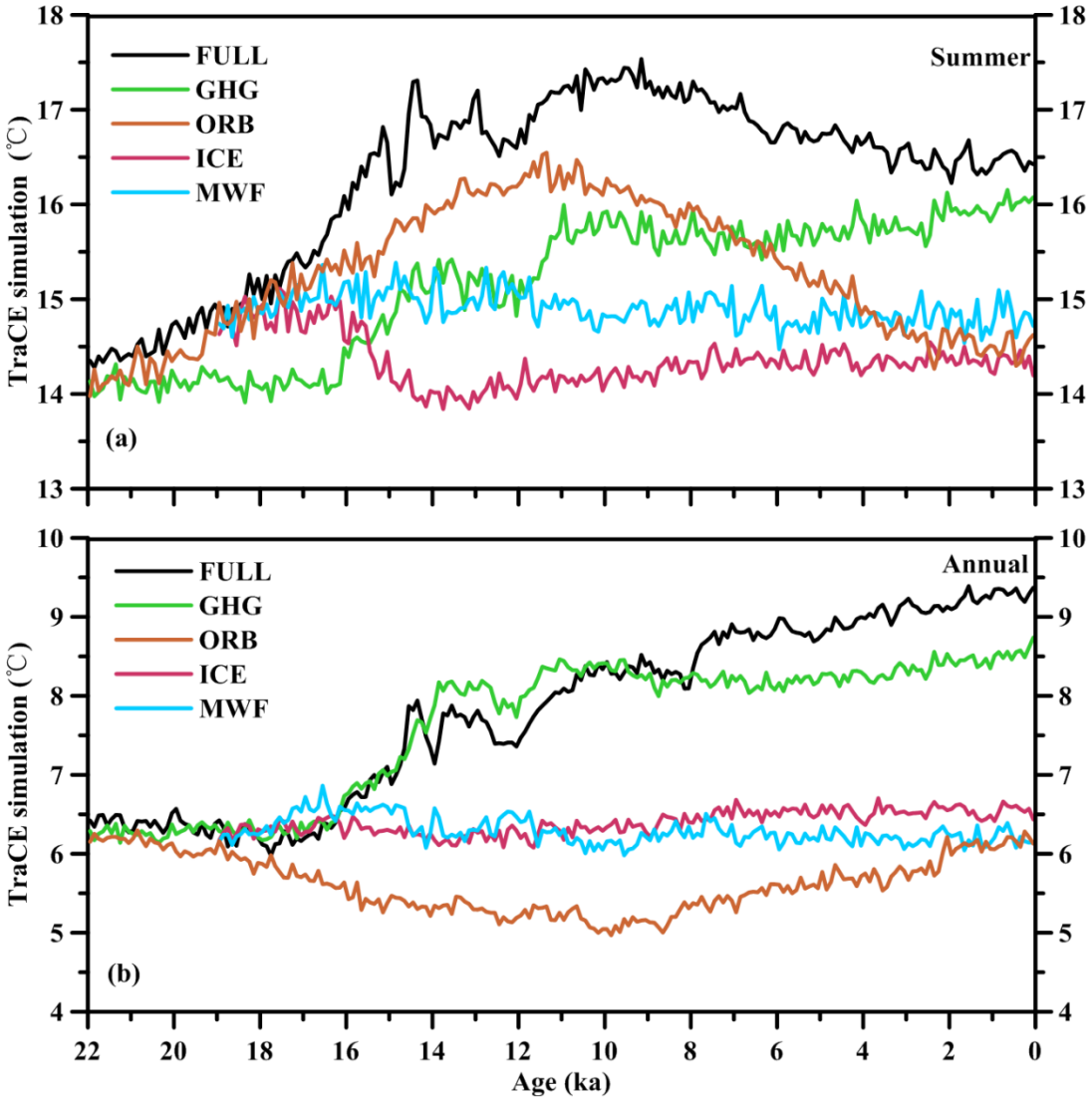

Fig. S10. TraCE simulated seasonal temperature with full and individual forcing. (**a**), TraCE outputs for summer temperatures at southwestern China indicating the dominant control of summer insolation. (**b**), TraCE outputs for annual mean temperatures indicating the dominant control of annual mean insolation. Each output contains full forcing (FULL, black) and individual forcings (greenhouse gas (GHG), green; orbital (ORB), earth yellow; ice sheet (ICE), cameo brown; melt water flux (MWF), cyan).

Table. S1. Location and environmental settings of southwestern Chinese lakes.

Lake	Latitude	Longitude	Elevation (m)	Area (km^2)	maximum water depth (m)	SW pH	DO (mg/L)	Conductivity (us/cm)	MAAT
Chenghai lake	24°17' N	102°45' E	1494	77.22	35.1	9.1	7.51	1130	17.4
Cuoqia lake	27°24' N	99°45' E	3960	0.084	26.4	6.67	3.74	9.5	3.2
Erhai lake	25°58' N	100°18' E	1969	249	20.7	8.5	7.59	280	15.9
Fuxian lake	24°38' N	102°58' E	1716	211	155	8.86	7	320	16.9
Lugu lake	27°45' N	100°50' E	2691	48.45	93.5	8.5	6.54	215	12.0
Tiancai lake	26°38' N	99°43' E	3880	0.02	7	7.45	0.502	11	3.7
Tingming lake	26°35' N	99°01' E	3779	1.5	19.2	6.8	1.84	-	4.3
Xingyun lake	24°24' N	102°49' E	1730	34.71	11	8.9	7	344	17.0
Tengchong qinghai lake	25°07'N	98°34' E	1885	0.25	8.1	5.8	7.2	11.8	16.0

Table S2. AMS-^{14}C radiocarbon dates from core TCQH17A).

Lab No.	Depth (cm)	Material	$\delta^{13}C$ (%VPDB)	^{14}C date (yr BP±2σ range)	Calibrated age (cal yr BP±2σ range)
Beta-473793	94	Plant fragments	-29.1	810±30	731±51
Beta-473794	144	Plant fragments	-29.9	2130±30	2080±79
Beta-473795	198	Plant fragments	-26.5	3910±30	4335±87
Beta-473796	308	Plant fragments	-29.6	7070±30	7902±58
Beta-473797	354	Plant fragments	NA	8310±30	9342±94
Beta-473798	435	Plant fragments	-27.5	10150±30	11856±156
Beta-473799	479	Plant fragments	-33.2	12020±40	13881±128
Beta-473800	593	Plant fragments	-30.2	16240±50	19438±192
Beta-473801	719	Plant fragments	-27.7	19180±60	23139±257
Beta-473802	789	Plant fragments	-26.3	22090±90	26310±265
Beta-531492	900	Organic matter	-25.0	27170±120	31135±192
Beta-531493	950	Organic matter	-24.5	29040±140	33250±395
Beta-531490	1008	Charcoal	NA	30610±180	34535±369